DESPECKLING AND CLASSIFICATION OF LIVER ULTRASOUND IMAGES

Project report submitted in partial fulfillment of the requirement for the degree of

MASTER OF TECHNOLOGY

IN

ELECTRONICS & COMMUNICATION ENGINEERING

UNDER THE GUIDANCE OF

Dr. JITENDRA VIRMANI

BY

NIMISHA MANTH (132019)

May 2015

JAYPEE UNIVERSITY OF INFORMATION TECHNOLOGY
Waknaghat, Solan, Himachal Pradesh– 173234

Candidate's Declaration

I hereby declare that the work titled **"Despeckling and Classification of liver Ultrasound images"** carried under the supervision of Dr. Jitendra Virmani in partial fulfillment for the award of degree of Master of Technology in Electronics and Communication Engineering to Jaypee University of Information Technology, Waknaghat-Solan has not been submitted partially or wholly to any other University or Institute for the award of this or any other degree or diploma.

Date: Signature of Student

This is to certify that the above statement made by the candidate is correct to the best of my knowledge.

Date: Signature of Supervisor

Acknowledgements

This project work is the most significant accomplishment of my life by far. I would like to extend my gratitude and heartfelt thanks to my supervisor Dr. Jitendra Virmani, Assistant Professor (Sr. Grade), Department of Electronics and Communication Engineering, Jaypee University of Information Technology, Waknaghat-Solan, for his constant support, encouragement, exemplary guidance and constructive criticism.

Date: Name and Signature of Student

Table of Contents

Chapter 3

Methodology

Chapter 4

Comparative analysis of Despeckle Filters for liver US images

Chapter 5

CAD System Design for Classification of Primary benign and Primary malignant FLLs

List of Figures

List of Tables

List of Acronyms

B-Mode	Brightness Mode
CAD	Computer-aided Diagnosis
CM	Confusion Matrix
CT	Computed Tomography
E3	Edge Detector Filter of Length 3
E7	Edge Detector Filter of Length 7
FLL	Focal Liver Lesion
FOM	Figure Of Merit
FOS	First Order Statistics
FPS	Fourier Power Spectrum
GB	Giga Byte
GHz	Giga Hertz
GLCM	Gray Level Co-occurrence Matrix
GLRLM	Gray Level Run Length Matrix
GWT	Gabor Wavelet Transform
HCAD	Hierarchical Computer-aided Diagnostic System
HCC	Hepatocellular Carcinoma
HEM	Hemangioma
ICA	Individual Class Accuracy
IQEMs	Image Quality Evaluation Metrics
IROIs	Inside Regions of Interest
L3	Level Detector Filter of Length 3
L7	Level Detector Filter of Length 7
LHCC	Large Hepatocellular Carcinoma

MET	Metastatic Carcinoma
ML	Malignant Lesion
MRI	Magnetic Resonance Imaging
NOR	Normal
OCA	Overall Classification Accuracy
PGIMER	Post Graduate Institute of Medical Education and Research
PSNR	Peak Signal to Noise Ratio
R3	Ripple Detector Filter of Length 3
R7	Ripple Detector Filter of Length 7
RAM	Random Access Memory
ROIs	Regions of Interest
S3	Spot Detection Filter of Length 3
S7	Spot Detection Filter of Length 7
SHCC	Small Hepatocellular Carcinoma
SROIs	Surrounding Regions of Interest
SSIM	Structure Similarity Index
SVM	Support Vector Machine
SSVM	Smooth Support Vector Machine
TDs	Texture Descriptors
TEI	Texture Energy Image
TFV	Texture Feature Vector
US	Ultrasound

The present research work has been carried out to enhance the diagnostic quality of conventional B-Mode ultrasound (US) imaging modality for diagnosis of liver diseases. The study was conducted by collecting a comprehensive image database of 151 B-Mode liver US images with representative cases from each image class, acquired from the patients who underwent US examination at the Department of Radiodiagnosis and Imaging, PGIMER, Chandigarh, India during a period from March 2010 to March 2012. The research objectives for the present work were formulated keeping in view the needs of the radiologists, based on the practical difficulties faced by them in routine clinical practice.

The image database comprises of 23 Normal (NOR), 14 Cirrhotic, 14 Cyst, 19 Hemangioma (HEM), 36 Hepatocellular Carcinoma (HCC) and 45 Metastatic Carcinoma (MET) liver images. Further bifurcation of Cyst, HEM and MET images into typical and atypical cases, and HCC cases into small HCC (SHCC) and large HCC (LHCC) cases is shown in Fig. 1.

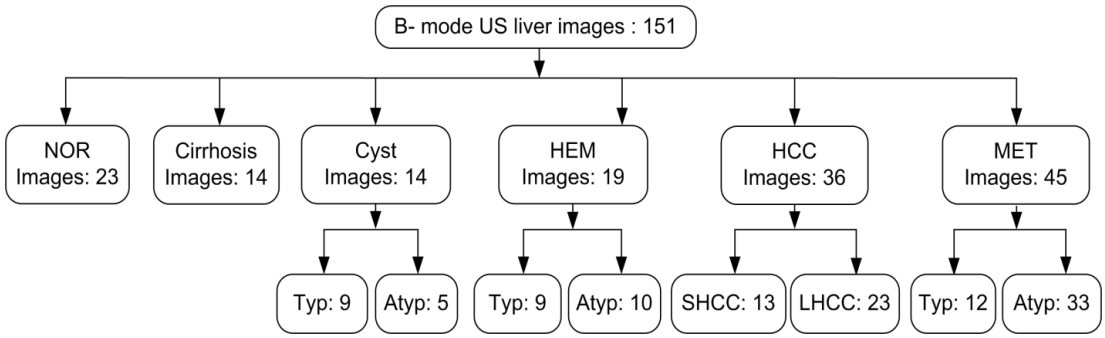

Fig. 1 The description of image database used in the present research work.
Note: NOR: Normal; HEM: Hemangioma; HCC: Hepatocellular carcinoma; MET: Metastatic carcinoma; SHCC: Small HCC; LHCC: Large HCC; Typ: Typical; Atyp: Atypical.

The differential diagnosis between atypical cases of Focal Liver Lesions (FLLs) is a daunting challenge even for experienced radiologists. Therefore, there is a significant impetus among the research community to develop computer aided diagnostic (CAD) systems for differential diagnosis between different cases of liver Ultrasound (US) images.

The proposed interactive system for diagnosis of liver diseases using B-Mode US images consists of two modules as shown in Fig. 2. *Module* 1 is designed to remove and speckle noise from the liver US images and evaluate the performance of

despeckled images with the help of Image Quality Enhancement Metrics (IQEMs). *Module* 2 is designed to assist or provide second opinion to the radiologist if there is confusion within benign and malignant liver image classes.

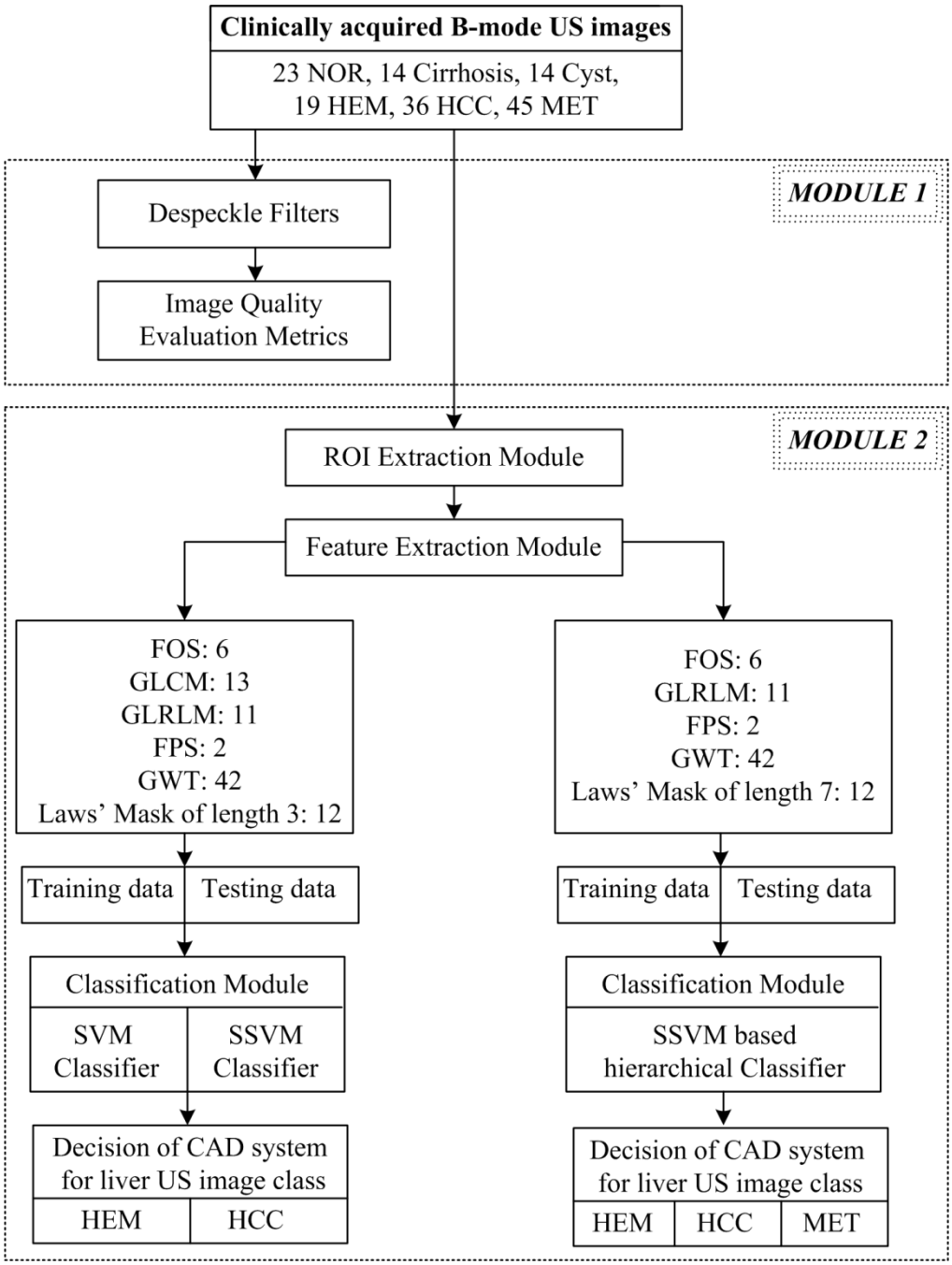

Fig. 1. Block diagram of the proposed interactive system for diagnosis of liver diseases.
Note: FOS: First order statistics, GLCM: Gray level co-occurrence matrix, GLRLM: Gray level run length matrix, GWT: Gabor wavelet transform, FPS: Fourier power spectrum, SVM: Support Vector Machine; SSVM: Smooth Support Vector Machine.

In *Module* 1, the performance of different despeckling algorithms with respect to (*a*) smoothening of homogeneous areas, (*b*) edge preservation, and (*c*) feature/ structure preservation for B-mode liver ultrasound images has been investigated. The study has been carried out on diversified image dataset consisting of images with (*a*) normal liver tissue, (*b*) cirrhosis, (*c*) cyst, (*d*) typical and atypical cases of hemangioma and metastatic carcinoma lesions, and (*e*) small and large hepatocellular carcinoma lesions.

Ten despeckling filtering algorithms, based on, local statistics, median filtering, geometric filtering and anisotropic diffusion have been applied on a real database of 151 conventional gray scale liver ultrasound images. As the sonographic appearances exhibited by small as well as large hepatocellular carcinoma, atypical cases of cyst, hemangioma and metastatic carcinoma are highly overlapping, the differential diagnosis between these malignant focal liver lesions is considered as a difficult task.

Therefore, in the present study, quantitative analysis has been carried out with respect to (*a*) smoothening of homogeneous areas (i.e. PSNR metric), (*b*) edge preservation (i.e. FOM index), and (*c*) feature/structure preservation (i.e. SSIM index). The exhaustive objective analysis carried out in the present study, illustrates that the image processed by Lee Sigma method based on Local Statistics yields the best results with respect to smoothing, edge and feature/ structure preservation.

Early diagnosis of liver cirrhosis using texture descriptors computed from regions of interest (ROI) extracted from conventional B-Mode liver US images is clinically significant as most of the cirrhotic patients are asymptomatic, and the biochemical tests like elevated liver enzyme detect cirrhosis at an advanced stage.

It is worth mentioning that the patients with liver cirrhosis are at high risk of developing hepatocellular carcinoma (HCC, a primary malignant focal liver lesion), and cirrhosis is also the leading cause of portal hypertension. Furthermore, since liver cirrhosis is considered as a pre-cursor to development of HCC and it is considerably difficult to diagnose small HCCs developed on already nodular cirrhotic liver parenchyma, the diagnosis as to whether the textural changes in the liver parenchyma are cirrhotic changes or they indicate the development of HCC is absolutely necessary.

It is worth mentioning that there is a considerable overlap between the sonographic appearances of HCC and MET lesions, at the same time the differential diagnosis between HCC and MET lesions is essential for effective treatment of liver malignancies.

Accordingly, the *Module* 2 of the proposed interactive system for diagnosis of liver diseases incorporates two different CAD systems: (*i*) CAD System-I for binary classification between primary benign and primary malignant liver lesions, and (*ii*) Hierarchical CAD System-II for classification between benign and malignant liver lesions.

The CAD Systems of *Module* 2 is designed to assist or provide second opinion to the radiologist for making differential diagnosis between benign and malignant lesions using B-Mode US images.

The radiologists diagnose typical FLLs easily by their classic sonographic appearances; however, the differential diagnosis between atypical FLLs from B-Mode US is quite a challenging task faced in routine clinical practice, mainly due to existence of overlapping sonographic appearances even within individual classes of FLLs. Even then, B-Mode US is considered as preferred examination for characterization of FLLs, mainly due to its noninvasive, nonradioactive, inexpensive nature and real-time imaging capabilities. Therefore, a CAD system for classification of FLLs from B-Mode US images is highly desired. At the same time, it is worth mentioning that there are certain disadvantages associated with the use of B-Mode US for characterization of FLLs: (*a*) limited sensitivity for detection of small FLLs (< 2 cm) developed on cirrhotic liver which is already nodular and coarse-textured, (*b*) sonographic appearance of HCC and MET lesions are highly overlapping, (*c*) sonographic appearances of cystic metastasis and atypical cyst are often overlapping, (*d*) sonographic appearances of atypical HEM, sometimes mimic with atypical MET or HCC, and (*e*) difficulty to characterize isoechoic lesions with very slim difference in contrast between region inside the lesion and the surrounding liver parenchyma in some cases.

As it is well known fact that US imaging has limited sensitivity for detection of SHCCs less than 2 cm in size, therefore in order to design a robust classification

system, it is ensured that the constituent HCC images in the dataset offered a high degree of variability in terms of size and sonographic features.

To ensure generality, the training data for designing the classifier was chosen carefully in consultation with experienced participating radiologists, so as to include all the typical and atypical image classes for HEM, and MET lesions as well as small and large HCC lesions for designing a robust classifier with representative cases for all image subclasses. Two sets of images were created for each image class, ROIs from one set of images were used for training and ROIs from the other set were used for testing to avoid any biasing.

Radiologists visualize the texture patterns of the regions inside and outside of the lesion for differential diagnosis between FLLs using B-Mode US images. Accordingly, texture feature extraction from IROIs as well as SROIs was considered for the design of the proposed CAD system. Thus, IROIs (extracted from the region inside the lesion) and a corresponding SROI (extracted from the surrounding of each lesion) are inputted to *Module* 2 for classification between benign and malignant liver image classes.

The region of interest (ROI) extracted by the radiologist, is fed to CAD system-I, in order to compute the texture descriptors from IROIs and SROIs using six feature extraction methods namely, FOS, GLCM, GLRLM, FPS, Gabor and Laws' mask of length 3. Three texture feature vectors (TFVs) i.e., TFV1 consists of texture features computed from IROIs, TFV2 consists of texture ratio features (i.e., texture feature value computed from IROI divided by texture feature value computed from corresponding SROI) and TFV3 computed by combining TFV1 and TFV2 (IROIs texture features + texture ratio features) are subjected to classification by SVM and SSVM classifiers. It is observed that the performance of SSVM based CAD system is better than SVM based CAD system with respect to (*a*) overall classification accuracy (*b*) individual class accuracy for atypical HEM class and (*c*) computational efficiency. The promising results obtained from the proposed SSVM based CAD system design indicates its usefulness to assist radiologists for differential diagnosis between primary benign and primary malignant liver lesions.

The CAD system II designs implemented in the present research work for characterization of benign and malignant lesions using B-Mode US images include

designs (*a*) SSVM based multiclass classifiers, and (*b*) using hierarchical framework of SSVM based binary classifiers. The first SSVM based classifier classifies the liver images into primary benign (i.e., HEM) and malignant (i.e., HCC and MET) cases. The malignant cases are further classified by second SSVM based classifier into primary malignant (i.e., HCC) and secondary malignant (i.e., MET) cases.

Chapter 1

Introduction

1.1 Motivation

Liver is the most vital and largest organ of human body. It performs various functions such as production and excretion of bile juice (i.e., a digestive fluid), production of fats, synthesis of cholesterol, metabolism of fats, proteins and carbohydrates, storage of minerals and vitamins, synthesis of plasma proteins, blood detoxification, blood pressure management, breakdown of insulin and other hormones, etc. Liver is a metabolically active organ necessary for survival.

As liver is the largest solid organ of human body, it becomes an easy target for many diseases. In clinical diagnosis, liver diseases are considered serious as it is a vital organ, which performs important functions of human body. Liver diseases are classified in two broad categories, i.e., diffuse liver diseases and focal liver diseases.

1.1.1 Diffuse Liver Diseases

In diffuse liver diseases, the abnormality is distributed throughout the liver tissue. Among diffuse liver diseases, the liver cirrhosis is considered more serious as it represents the end stage of chronic diffuse liver disease. The viral hepatitis (such as hepatitis B or C) is one of the causes of liver cirrhosis; the virus can induce chronic inflammation in the liver causing fibrotic changes. The extent of fibrosis in liver tissue can range from fibrous expansion in the portal area to cirrhosis.

In liver cirrhosis, strong association with fibrosis results in regenerative nodule formation which leads to alterations in normal hepatic structure such as (*a*) decrease in homogeneity, (*b*) modification in hepatic vessels, (*c*) modification in shape and contour, and (*d*) increase in liver volume (i.e., toxic cirrhosis) or decrease in liver volume (i.e., viral cirrhosis).

Since fibrosis is a necessary stage that leads to cirrhosis which is an irreversible process, therefore, it is critical to detect the fibrosis status at an early stage so that proper medication is administered to avoid cirrhosis.

1.1.2 Focal Liver Diseases

In focal liver diseases, the abnormality is concentrated in a small localized region of the liver parenchyma which is often referred to as focal liver lesion (FLL). Liver Cysts, HEM (i.e., primary benign FLL), HCC (i.e., primary malignant FLL) and MET (i.e., secondary malignant FLL), are some of the commonly occurring focal liver diseases.

1.1.2.1 Liver Cyst

Liver Cysts are most common FLLs, and are frequently observed on US. Cysts represent the fluid filled cavities in the liver. Usually, cysts are asymptomatic unless they are large enough to cause mass effect (i.e., displacement and compression of adjacent structures). Mostly, liver cysts are incidental findings during the US scan. Typical cysts appear with anechoic echotexture, well defined smooth thin lined capsule and posterior acoustic enhancement. On the other hand, atypical cysts contain low level fine echoes which occur as a result of hemorrhage or infection and are outlined by thick irregular wall. These atypical cysts are usually asymptomatic; however, the symptomatic ones are regularly monitored on US and treated with percutaneous aspiration under US guidance or laparoscopic unroofing. Typical cysts can be easily diagnosed from their characteristic appearance on B-Mode US, but atypical cysts can be easily confused with cystic metastasis. Atypical cysts always appear with thickened irregular walls and internal echoes. Differential diagnosis of cystic metastasis and atypical cyst using conventional gray scale B-Mode US can be quite challenging.

1.1.2.2 Hemangioma (HEM)

The hemangioma (HEM) is the most common primary benign FLL [1- 5]. HEMs usually appear as a solitary lesion, but may also be multiple in 10 % of cases. In very rare cases, these lesions are symptomatic; but it is sometimes difficult to diagnose these lesions as they can be indistinguishable from MET lesions [1, 6- 9].

In 70 % of cases, HEMs encountered in routine clinical practice are typical HEMs. These typical HEMs have a characteristic sonographic appearance; it appears as a round, homogeneous, hyperechoic, well defined lesion [1, 2, 8- 11]. Atypical HEMs are difficult to diagnose as they are a great impersonator [1]. The sonographic appearance of atypical HEMs can be hypoechoic or isoechoic which resembles to that of atypical METs and HCC lesions [1, 6- 9]. These atypical HEMs generally cause diagnostic problems as they may

appear as hypoechoic lesions or as lesions with mixed echogenicity. In case of atypical HEMs, where the diagnosis is not certain and a malignancy is suspected, administration of an ultrasound contrast agent and further imaging like MRI scanning helps to characterize the lesion confidently.

1.1.2.3 Hepatocellular Carcinoma (HCC)

The hepatocellular carcinoma (HCC), also called as malignant hepatoma (liver cancer), is primary malignant FLL [1, 2, 8, 10- 15]. HCC accounts for 80 to 90 % of all the malignant FLLs, amongst various primary FLLs [16- 18]. The US imaging modality is used world-wide for screening of HCCs.

The risk factors which give rise to development of HCC are (*a*) cirrhosis, (*b*) chronic infection with the hepatitis B and hepatitis C virus, and (*c*) metabolic diseases. In 85 % cases, HCC occurs in patients with cirrhosis [1, 2, 8, 10- 15]. The appearance of HCC on B-Mode US depends mostly on whether or not there is underlying cirrhosis. In fact, in radiology practice, cirrhosis is seen as precursor to development of HCC as the occurrence of HCCs on normal liver is very rare [1, 10, 13, 14]. Detecting small HCCs (SHCCs) developed on coarse and nodular cirrhotic liver parenchyma presents a daunting challenge for experienced radiologists [1, 7, 12, 19].

The sonographic appearance of a large HCC (LHCC) is often inhomogeneous, whereas SHCCs can be hypoechoic and homogeneous [1, 9, 11]. Experienced participating radiologists opined that no sonographic appearance can be considered typical for HCC as there is a wide variability of sonographic appearances even within SHCCs and LHCCs. The sonographic appearances of SHCC vary from hypoechoic to hyperechoic [9] while LHCC appear frequently with mixed echogenicity [1, 11].

1.1.2.4 Metastasis (MET)

The Metastasis or Metastatic carcinoma (MET) is the most common secondary malignant FLL [1, 2, 3, 8, 9, 12]. MET is caused by the cancerous cells that spread from the primary cancerous tumours of the other parts of the body. As the liver is the largest solid organ of the human body, it becomes an easy target for occurrence of metastatic tumors. Metastatic tumours are common during the late stages of cancer. MET may occur singly or as multiple deposits of varying sizes.

The sonographic appearance of typical MET lesion is the target or bull's-eye appearance (i.e., hypoechoic centre surrounded by a hyperechoic rim) [2, 3, 7, 8, 10, 12,]. Atypical MET lesions can appear with extremely variable sonographic appearances ranging from anechoic, hyperechoic, isoechoic, hypoechoic, and even with mixed echogenicity. The Differential diagnosis between atypical MET lesions from certain HEM and HCC lesions is considerably difficult [1, 2, 7, 8, 9, 21].

1.1.3 Ultrasound Imaging

The field of medical imaging and image analysis has evolved due to collective efforts from many disciplines like engineering, medicine and basic sciences. In current medical practice, imaging procedures are one of the major bases for diagnosis apart from other procedures like pathological examinations and biopsy. The overall objective of the medical imaging system is to acquire useful information about the physiological processes of the organs of the human body. The other imaging modalities used for diagnosis of liver diseases include computed tomography (CT) and magnetic resonance imaging (MRI). The US, CT and MRI are all non-invasive imaging modalities. However, CT uses ionizing radiations, which are otherwise harmful for human body. On the other hand, US don't produce any known harmful effects on any of the tissues examined during clinical practice. The clinical relevance of the US imaging modality is high worldwide due to its versatility, wide spread availability, portability and ease of operation in comparison to CT and MRI.

The US imaging modality is the first choice for the diagnosis of liver disease due to its inexpensive, non-invasive and non-radioactive nature and real time imaging capabilities [3, 10, 13, 23- 25]. The other imaging techniques like MRI, CT etc. offer high sensitivity in comparison to B-mode (i.e. conventional gray scale) US for FLL characterization, but they are not widely available and are expensive [1, 4, 10, 11, 13, 14, 21, 26, 27].

1.2 Sonographic Appearances of Different Liver Image Classes used in the Present Research Work

The brief details of the sonographic appearances of liver image classes used in the present research work are depicted below:

1.2.1 Sonographic Appearance of Normal (NOR) Liver

The sample of the Normal (NOR) liver image from the image database is given in Fig. 1.1.

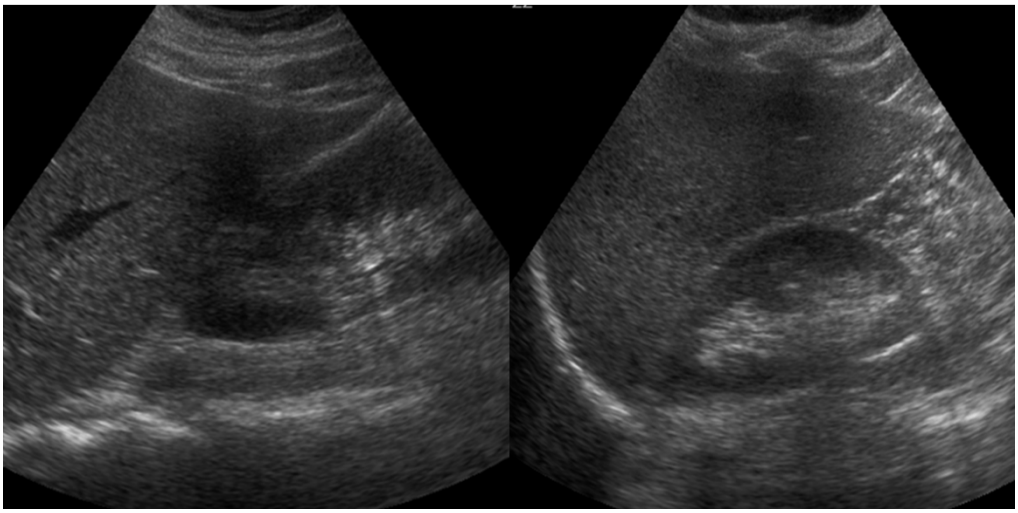

Fig. 1.1 Conventional gray scale ultrasound liver images with appearance of normal liver.
Note: Normal liver exhibits homogeneous echotexture with medium echogenicity.

Fig. 1.1. The sonographic appearance of normal (NOR) liver is homogeneous with slightly increased echogenicity as compared to the right kidney [19, 25, 28]. The NOR liver appears as a mid gray organ with homogeneous echotexture and smooth outlining. The smooth liver parenchyma is interrupted by anechoic structures such as vessels, etc. The capsule of the liver appears hyperechoic especially at its border with the diaphragm. The diaphragm appears as a curvilinear bright reflector. It is difficult to quantify the size of the liver as there are large variations in shape within normal subjects. The size of the liver is therefore assessed subjectively. All the NOR cases are considered as typical as there is no atypical appearance for normal liver tissue.

1.2.2 Sonographic Appearance of Cirrhotic Liver

The sample images of the cirrhotic liver from the image database are given in Fig.1.2.

The cirrhotic liver exhibits coarse echotexture with diffused uneven nodularity [1, 10, 25]. Variation in size and shape of liver is observed depending upon severity of the liver cirrhosis. The right lobe is mostly affected by cirrhosis. It is clinically believed that changes in the process of normal liver progressing towards cirrhosis can be related to echotextural changes in the liver parenchyma.

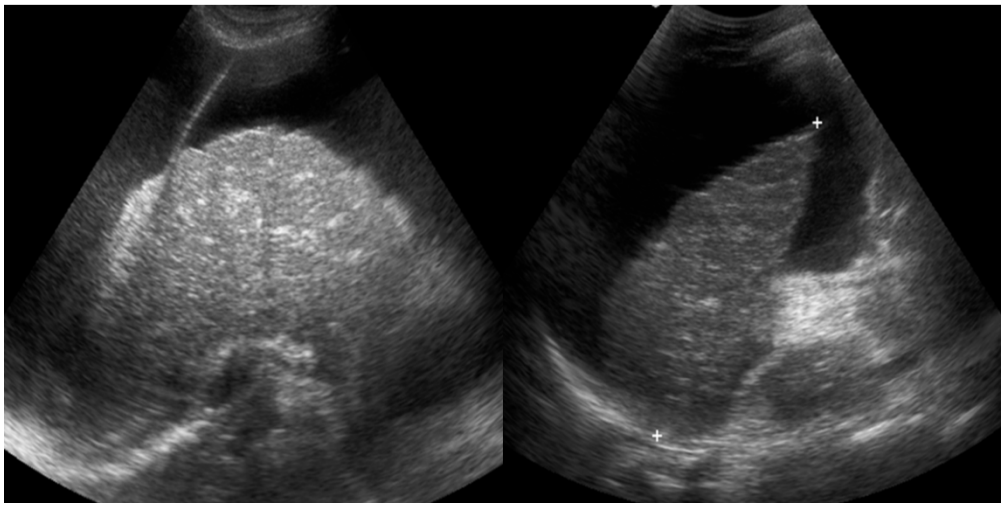

Fig. 1.2 Conventional gray scale B-Mode liver ultrasound images with appearance of cirrhotic liver. **Note:** Cirrhotic liver exhibits coarse echotexture with diffused uneven nodularity.

1.2.3 Sonographic Appearance of Typical FLLs

The sample images of typical case of Cyst, HEM and MET lesions from the image database are shown in Fig. 1.3.

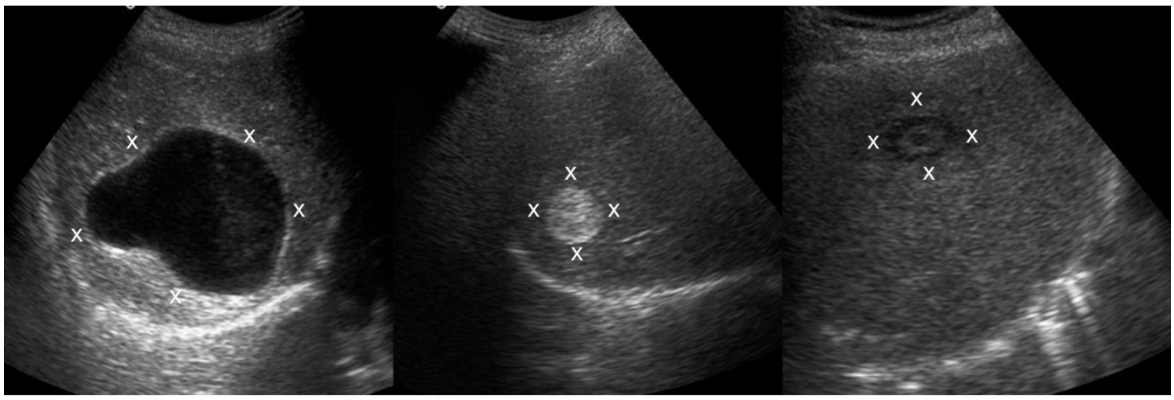

(*a*) (*b*) (*c*)

Fig. 1.3 Conventional gray scale US liver images: (*a*) Typical cyst (thin walled anechoic lesion with posterior acoustic enhancement); (*b*) Typical HEM (well circumscribed uniformly hyperechoic appearance); (*c*) Typical MET (target or bull's-eye appearance i.e. hypoechoic centre surrounded by a hyperechoic rim).

Typical cyst appears as round, anechoic lesion with posterior acoustic enhancement and well defined thin imperceptible wall. Typical HEM always appears as a well circumscribed uniformly hyperechoic lesion. The typical sonographic appearance of MET lesion is the target or bull's-eye appearance (i.e., hypoechoic centre surrounded by a hyperechoic rim) [2, 3, 7, 8, 10, 12,].

1.2.4 Sonographic Appearance of Atypical FLLs

The sample images for atypical case of Cyst, HEM and MET lesion are shown in Fig. 1.4. Atypical cysts always appear with internal echoes and thickened irregular walls. Atypical HEMs are a great mimic and definite diagnosis with conventional gray scale B-

Mode US is difficult [1]. Atypical HEMs can be isoechoic or even hypoechoic mimicking the sonographic appearance of certain atypical MET and HCC lesions. Atypical MET lesions can appear with extremely variable sonographic appearances ranging from anechoic, hyperechoic, isoechoic, hypoechoic and even with mixed echogenicity. Differentiating atypical MET lesions from certain HEM and HCC lesions is considerably difficult [1, 2, 7, 8, 9, 21].

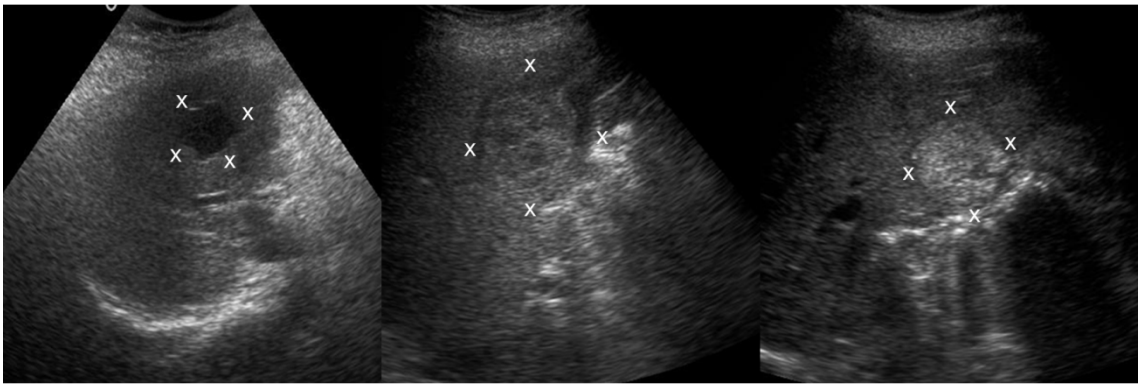

(*a*) (*b*) (*c*)

Fig. 1.4 Sample image variants with appearance of : (*a*) Atypical cyst with internal echoes and irregular walls; (*b*) Atypical HEM with heterogeneous echotexture; (*c*) Hyperechoic atypical MET with heterogeneous echotexture.

1.2.5 Sonographic Appearance of Small and Large HCCs

The sample images of SHCC and LHCC cases from the image database are shown in Fig. 1.5. The sonographic appearances of Small HCC (SHCC) vary from hypoechoic to hyperechoic [9]. Large HCC (LHCC) appears frequently with mixed echogenicity [1, 11]. Experienced participating radiologists opined that no sonographic appearance can be considered typical for HCC as there is wide variability of sonographic appearances even within SHCCs and LHCCs.

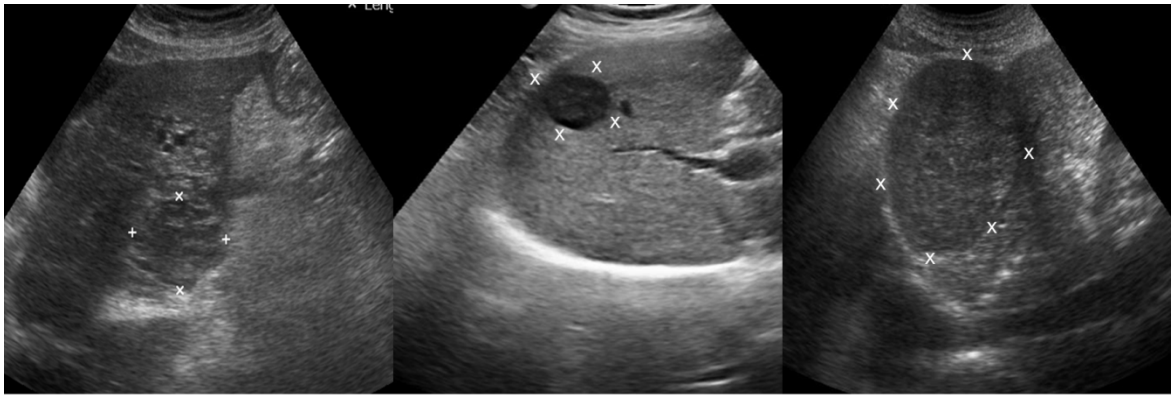

(*a*) (*b*) (*c*)

Fig. 1.5 Sample images of SHCC and LHCC variants from the image database: (*a*) small HCC with mixed echogenicity; (*b*) small HCC with hypoechoic appearance; (*c*) large HCC with mixed echogenicity.

1.3 Need for Despeckle filtering for B-Mode Liver Ultrasound images

Speckle noise (also known as multiplicative noise) corrupts the medical US image, thereby, making it difficult for visual observation [29- 31]. The objective of despeckling an ultrasound image is to smoothen the homogeneous areas while preserving the edges and structural information so that the diagnostic features present in the image are highlighted. In the present work, different despeckling methods i.e., methods based on local statistics, median filtering, geometric filtering and anisotropic diffusion have been used. The performance of different despeckling algorithms with respect to (*a*) smoothening of homogeneous areas, (*b*) edge preservation, and (*c*) feature/ structure preservation for B-mode liver ultrasound images has been investigated. As the sonographic appearances exhibited by small as well as large hepatocellular carcinoma, atypical cases of cyst, hemangioma and metastatic carcinoma are highly overlapping, the differential diagnosis between these malignant focal liver lesions is considered as a difficult task. Therefore, in the present study, quantitative analysis has been carried out with respect to (*a*) smoothening of homogeneous areas (Peak Signal to Noise Ratio i.e. PSNR metric) [32], (*b*) edge preservation (Figure of Merit i.e. FOM index) [33, 34], and (*c*) feature/structure preservation (Structure Similarity Index i.e. SSIM index) [35].

1.4 Need for CAD Systems for Liver Diseases using B-Mode Ultrasound Images

The evolution of computer technology, medical image processing algorithms and artificial intelligence techniques has given ample opportunity to researchers to investigate the potential of computer-aided diagnostic systems for tissue characterization. Tissue characterization refers to quantitative analysis of tissue imaging features resulting in accurate distinction between normal and abnormal tissues. Thus, the result of tissue characterization is interpreted using numerical values. The overall aim of developing a computerized tissue characterization system is to provide additional diagnostic information about the underlying tissue which cannot be captured by visual inspection of B-Mode US images.

Ultrasonographic tissue characterization methods based on physical tissue models have been shown to be useful for improving the diagnostic accuracy of sonograms. Unfortunately, no physical model based diagnostic system have been developed for characterization of FLLs probably because these systems have been developed assuming

single, homogeneous tissue model, whereas in case of FLLs the variability in sonographic appearances within different lesions is quite large and quite often large HCCs and MET lesions are inhomogeneous [1, 2, 7, 8, 9, 21].

1.5 Objectives of the Present Study

The main objective of the research work presented in this thesis is to enhance the diagnostic potential of conventional gray scale B-Mode ultrasound for diagnosis of liver diseases by removing speckle noise from the US images and by developing efficient CAD system designs using a comprehensive and representative image database. To achieve this, various research objectives were formulated according to the needs of the radiologists, based on the practical difficulties faced by them in routine clinical practice. These research objectives are described below:

(*i*) *The collection of a comprehensive and representative image database*: In order to develop efficient and robust classifier designs, it is necessary to train the classifiers with a comprehensive image database with representative images from each subclass. Thus, collection of a comprehensive image database with representative cases from each class, including (*a*) NOR liver, (*b*) cirrhotic liver, (*c*) typical and atypical cases of cyst, HEM and MET lesions and (*e*) small as well as large HCC cases is taken up as the first objective of the present research work.

(*ii*) *The implementation of despeckling filters and performance evaluation of B-Mode US images*: In the present work, different despeckling methods i.e., methods based on local statistics, median filtering, geometric filtering and anisotropic diffusion have been used. The performance of different despeckling algorithms with respect to (*a*) smoothening of homogeneous areas, (*b*) edge preservation, and (*c*) feature/ structure preservation for B-mode liver ultrasound images has been investigated. As the sonographic appearances exhibited by small as well as large hepatocellular carcinoma, atypical cases of cyst, hemangioma and metastatic carcinoma are highly overlapping, the differential diagnosis between these malignant focal liver lesions is considered as a difficult task. Therefore, in the present study, quantitative analysis of has been carried out with respect to (a) PSNR metric (for smoothening of homogeneous areas) [32], (b) FOM index (for edge preservation) [33, 34], and (c) SSIM index (for feature/structure preservation) [35], is taken up as the first objective of the present research work.

(*iii*) *The design, development and implementation of an efficient CAD system for primary benign and primary malignant liver lesions using B-Mode US images*: The sonographic characterization of HEM (i.e., primary benign FLL) and HCC (i.e., primary malignant FLL) presents a daunting challenge for radiologists, due to their highly overlapping sonographic appearances [1, 2, 7, 8, 9, 21]. As the characterization of atypical HEM and HCC lesion is clinically significant for effective treatment, the design of an efficient CAD system for binary classification between HEM and HCC lesions by using a comprehensive and representative image database consisting of (*a*) typical and atypical MET cases, and (*b*) SHCC and LHCC cases, is taken up as the second objective of the present research work.

(*iv*) *The design, development and implementation of an efficient hierarchical CAD system for benign and malignant liver lesions using B-Mode US images*: The CAD system designs with hierarchically placed classifiers provide the possibility to go stepwise from the general classification problem, which is the identification of exact liver abnormality.

The design of hierarchical classifier is based on the idea of splitting the original problem of classifying the liver tissue in two sub-problems (*i*) diagnosis between primary benign and malignant lesions, and (*ii*) diagnosis of primary malignant and secondary malignant lesions. To develop an efficient hierarchical CAD system with texture features computed from regions inside and outside the lesions for diagnosis of FLLs using B-Mode liver ultrasound images is taken up as the third objective of the present research work.

1.6 Organization of Thesis

This thesis report is organized into seven chapters, as described below.

(*i*) *Chapter* 1 lays the foundation as to why 'Despeckling and Classification of B-Mode Liver Ultrasound Images' is clinically significant. It begins with documenting facts like why liver diseases are considered seriously? What types of liver diseases are most common? How these diseases affect the sonographic appearance of the liver tissue? Why B-Mode ultrasound examination is considered as primary choice for diagnosis of liver diseases? What are the problems faced by the radiologists for diagnosis of liver diseases using B-Mode ultrasound which are encountered in clinical practice? What is the speckle noise and why is it necessary to remove it?

Why there is a need to develop efficient CAD systems for diagnosis of liver diseases using B-Mode US images? What are the objectives of the present research work? How these objectives were formulated? To conclude, the content documented in this chapter provides the basic motivation regarding the fact that computer vision for liver US images can enhance the diagnostic potential of B-Mode US imaging modality.

(*ii*) *Chapter* 2 presents a brief literature review of the other related studies for diagnosis of liver diseases using B-Mode ultrasound images.

(*iii*) *Chapter* 3 lays the foundation of research methodology followed for undertaking this research work. The importance of medical ethics, while working with clinical human data is highlighted. The Chapter introduces the readers, to various set of protocols followed for undertaking this research work, i.e., the protocols followed for collection of comprehensive and representative image database, for assessment of images, for selection of ROIs, for selection of ROI size, for bifurcation of dataset into training dataset and testing dataset. Thus, the complete description of dataset used in the present research work is described in this Chapter.

(*iv*) *Chapter* 4 gives a detailed description of Despeckle filters and Image Quality Evaluation Metrics (IQEMs) for the removal of speckle noise and its performance evaluation using B-Mode liver US images.

(*v*) *Chapter* 5 provides description of the proposed CAD system for characterization of primary benign and primary malignant liver lesion.

(*vi*) *Chapter* 6 reports the experimentation carried out to design an efficient hierarchical CAD (HCAD) system for focal liver lesions using hierarchically placed classifiers.

(*vii*) .*Chapter* 7 summarizes the conclusions drawn from the exhaustive experimentation carried out in the present research work on “Despeckling and Classification of B-Mode Liver US Images”. The future directions in which the work can be extended are also reported in this Chapter.

Chapter 2

Literature Review

2.1. Literature Review for Despeckle Filtering

Speckle noise (also known as multiplicative noise) corrupts the medical US image, thereby, making it difficult for visual observation [29- 31]. The despeckling filtering algorithm can be classified based on (*a*) local statistics, (*b*) median filtering, (*c*) geometric filtering, and (*d*) anisotropic diffusion. The research works reported in related studied have used various filters for despeckling. An overview of Despeckle filtering techniques used in the present work is tabulated in Table 2.1.

Table 2.1. An overview of despeckle filtering techniques used in the present work.

Speckle reduction technique	Investigators	Method	Filter name
Local statistics based filtering	[36- 40]	Moving window using local statistics a) mean (m), variance (σ^2)	dsf-lsmv
	[36, 37]	b) Lee filters.	dsf-Lee
	[41]	c) Lee's Sigma filters.	dsf-Leesig
	[42]	d) Enhanced Lee filters.	dsf-enLee
	[43, 44]	e) Kaun filters.	dsf-Kaun
	[38]	f) Frost filters.	dsf-Frost
Median filtering	[45]	Median filtering.	dsf-median
Geometric filtering	[46, 47]	Nonlinear iterative algorithm.	dsf-gf
Diffusion based filtering	[38, 48- 52]	a) Nonlinear filtering technique for simultaneously performing contrast enhancement and noise reduction. Exponential damp kernel filters using diffusion.	dsf-ad
	[51]	b) Speckle reducing anisotropic diffusion filtering	dsf-srad

A brief description of the related studies is given as follows.

The despeckle filter- Kaun [43, 44] (dsf-Kaun) is a generalization of the despeckle filter- Lee [36, 37] (dsf-Lee), with the same structure. In both these filters, the average intensity of pixel values and a coefficient of variation in the moving window are used to compute the intensity of central pixel of the moving window.

The despeckle filter- Frost [38] (dsf-Frost) maintain the equivalence between the all-pass and averaging filters by using a convolution kernel which readjust itself in the areas containing edges.

The despeckle filter- median [45] (dsf-median) uses a nonlinear operator that alters the middle pixel, in the moving window with median value of the neighbors. The despeckle filter- geometric [46, 47] (dsf-gf) uses a nonlinear iterative algorithm, which increments or decrements the neighbor's pixel value depending on their relative values.

The despeckle filter- anisotropic diffusion [38, 48- 52] (dsf-ad) and the despeckle filter- speckle reducing anisotropic diffusion [51] (dsf-srad) are based on nonlinear filtering techniques which perform noise reduction and contrast enhancement by using the coefficient of variation [51].

The performance of different despeckling algorithms with respect to (*a*) smoothening of homogeneous areas, (*b*) edge preservation, and (*c*) feature/ structure preservation for B-mode liver ultrasound images, as these indices are considered as important for evaluation. The IQEMs, which includes, (*a*) PSNR metric (for smoothening of homogeneous areas) [32], (*b*) FOM index (for edge preservation) [33, 34], and (*c*) SSIM index (for feature/structure preservation) [35], have been computed for the pre-processed images. These image quality metrics depend on mutual information between the original and despeckled images and their natural scene statistics, has recently been used by Gupta *et al.* [53].

2.2 Literature Review for Classification

In literature, there are only few related studies on classification of FLLs. The brief description of these studies is given in Table 2.2.

Table 2.2. Studies on classification of FLLs using B-Mode Liver US images.

Studies	Liver image class	No. of ROIs	ROI size (pixels)	Classifiers used
[54]	NOR/HEM/Malignant	113	10 × 10	NN/LDA
[55]	NOR/Cyst/HEM/Malignant	120	10 × 10	NN
[7]	HCC/MET	174 (120 IROIs,54 SROIs)	32 × 32	SVM
[2]	NOR/Cyst/HEM/HCC/MET	491 (380 IROIs,111 SROIs)	32 × 32	KNN/PNN/BPNN
[8]	NOR/Cyst/HEM/HCC/MET	491(380 IROIs, 111SROIs)	32 × 32	SVM
[24]	NOR/Cyst/HEM/HCC/MET	491 (380 IROIs, 111 SROIs)	32 × 32	Ensemble of NN classifiers
[9]	HEM/Malignant	193	64 × 64	NN

Note: The HCCs evolved on cirrhotic liver only are considered as the occurrence of HCC on normal liver is rare; Nor: Normal; HEM: Hemangioma (primary benign lesion); HCC: Hepatocellular carcinoma (primary malignant lesion); MET: metastatic carcinoma (secondary malignant lesion).

The study in [54] used regions of interest (ROIs) of size 10 × 10 for computing gray-level run length matrix (GLRLM) and first order statistics (FOS) features to classify normal (NOR), HEM and malignant liver lesions by using neural network (NN) and linear discriminant analysis (LDA) classifier. The study in [55] computed texture features based on autocorrelation, gray level co-occurrence matrix (GLCM), edge frequency and Laws'

mask analysis from ROI of size 10 × 10 for the classification of NOR, Cyst, HEM and malignant liver lesions by using neural network classifier.

The research work carried out in study [7] used ROI of size 32 × 32 for computing GLCM, GLRLM, FPS, and Laws' texture features to classify HCC and MET lesions by using support vector machine (SVM) classifier. The research work in [7] has been carried out on 174 ROIs which includes 120 IROIs and 54 SROIs.

In studies [2, 8], five class classification between NOR, Cyst, HEM, HCC and MET classes has been carried out considering the ROI size of 32 × 32 pixels using KNN, PNN, BPNN and SVM classifiers. The research work in [2, 8] has been carried out on 491 ROIs including 380 IROIs and 111 SROIs.

The study in [24] reports five class classification between NOR, Cyst, HEM, HCC and MET classes considering two stage classification approach using 11 neural network classifiers. In first stage a single five class NN was used for prediction of probability of each class and in the second stage 10 binary NN classifiers were used. Based on the first two highest probabilities predictions of the first stage five class NN, the testing instance was passed to the corresponding binary NN of the second stage. The research work reported in [24] computed the texture features based on FOS, GLCM, GLRLM, FPS, Gabor Wavelet Transform (GWT) and Laws' features with the help of 491 ROIs including 380 IROIs and 111 SROIs.

However, the study in [9] reports the binary classification of HCC and HEM, HCC and MET, and MET and HEM lesions by computing the single-scale and multiscale texture features of 64 × 64 sized ROIs by using NN classifiers. The research work in [9] has been carried out on 193 ROIs.

It is highlighted in other studies that minimum 800 pixels are required to compute reliable estimates of statistical features [56- 58]. However, the research work reported in [54] and [55] has been carried out on ROI of size 10 × 10 which yields smaller number of pixels. The studies [2, 7, 8] used an ROI size of 32 × 32 and Yoshida et al. [9] used the ROI size of 64 × 64. Since, necrotic areas within the lesions should be avoided for cropping of inside ROIs (i.e., IROIs) and inhomogeneous areas include blood vessel etc. should be avoided for cropping of surrounding ROIs (i.e., SROIs), so in the present work, considering ROI size larger than 32 × 32 was not feasible. In studies [9, 54, 55] texture features of IROIs were only considered and the dataset description as to how many typical

and atypical HEMs and how many SHCC and LHCC were taken into consideration is not described.

2.3 Concluding Remarks

The Despeckle filters are generally categorized as local statistics filters, non-linear filter, and diffusion filters. Accordingly, in the present work six local statistics filters (i.e., Local statistics mean variance filter, Lee filter, Lee sigma filter, Enhanced Lee filter, Kaun filter and Frost filter), two non-linear filters (i.e., Median filter and Geometric filter), and two diffusion based filters (i.e., Anisotropic diffusion and Speckle Reduction Anisotropic Diffusion filter) have been used. It was observed that US liver images processed by Lee-Sigma despeckling algorithm results in better edge and structure preservation while providing adequate smoothing in the uniform areas.

From the literature, it has been concluded that the shape based features do not provide any significant information for differential diagnosis of FLLs. Accordingly, the present research work is based on the textural features only. The texture feature extraction methods are generally classified into statistical, spectral and spatial filtering based methods. The differential diagnosis between primary benign and primary malignant has not been done yet in the research field, therefore, this task has been carried out in the present work.

Chapter 3

Methodology

3.1. Introduction

From the extensive literature survey presented in the previous chapter, it can be observed that most of the related studies carried out in the past are based on the pre-processing of US images to remove the speckle noise. In the present thesis work, primarily two objectives have been met: (*a*) Comparative analysis of Despeckle filters for liver US images, (b) Design of CAD systems from B-Mode liver US images as shown in Fig. 3.1. The methodology for meeting the above two objectives is given below.

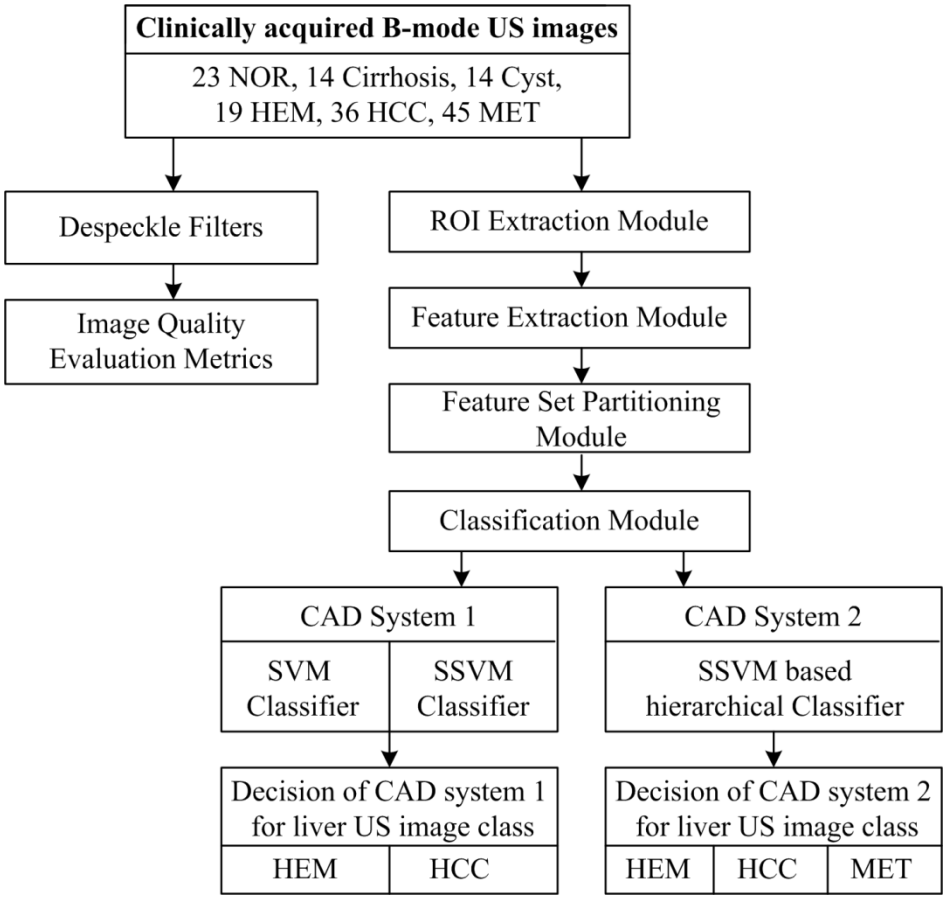

Fig. 3.1. The two main objectives of the thesis are divided into three categories as shown in the workflow.

3.2 Materials

3.2.1 Data Collection

In order to carry out the present research work, the B-mode liver US images were collected from the Department of Radiodiagnosis and Imaging, Post Graduate Institute of

Medical Education and Research (PGIMER), Chandigarh, India over the time period from March 2010 to December 2011. Informed consent of patients for using these images for research was taken prior to recording. The medical ethics board of PGIMER, Chandigarh, granted the ethical clearance to carry out this research work. The digital images were recorded by using Philips ATL HDI 5000 US machine equipped with multifrequency transducer of 2-5 MHz range were used. The size of the images is 800 × 564 pixels with gray scale consisting of 256 tones, and horizontal as well as vertical resolution is 96 dpi.

3.2.2 Data Collection Protocol

The following protocols were followed for data collection:

(*a*) The judgment regarding the representativeness and diagnostic quality of each image was made by two participating radiologists with 15 and 25 years of experience in US imaging. (*b*) The ground truth of Cirrhosis, Cyst, HEM, HCC, and MET lesions was confirmed using liver image assessment criteria including: (*i*) visualization of sonographic appearances, imaging features of lesions based on their expertise and knowledge, (ii) follow-up of clinical history of the patient and other associated findings and (iii) imaging appearance on magnetic resonance imaging (MRI)/ dynamic helical computed tomography (CT)/ pathological examinations and biopsy, which is an invasive procedure. (*b*) Only HCCs developed on cirrhotic liver are considered for analysis as the existence of HCCs on normal liver is rare. (*c*) The differentiation between LHCC and SHCC (i.e. ≤ 2 cm) was made by measuring the lesion size in longitudinal and transverse views.

3.2.3 Selection of Regions of Interest (ROIs)

In the present study, two types of ROIs i.e., inside regions of interest (IROIs) and surrounding regions of interest (SROIs) are used. The sample images of HEM and HCC cases with ROIs marked are shown in Fig. 3.2. The cropping of ROIs from image dataset has been done according to the following protocols:

(*a*) For cropping of IROIs, maximum non-overlapping IROIs were cropped from the region well within the boundary of each lesion by avoiding the necrotic areas, if any.
(*b*) For every lesion, one SROI was cropped from the surrounding liver parenchyma approximately from the same depth as that of the center of the lesion by avoiding the inhomogeneous structures such as blood vessels and liver ducts, etc.

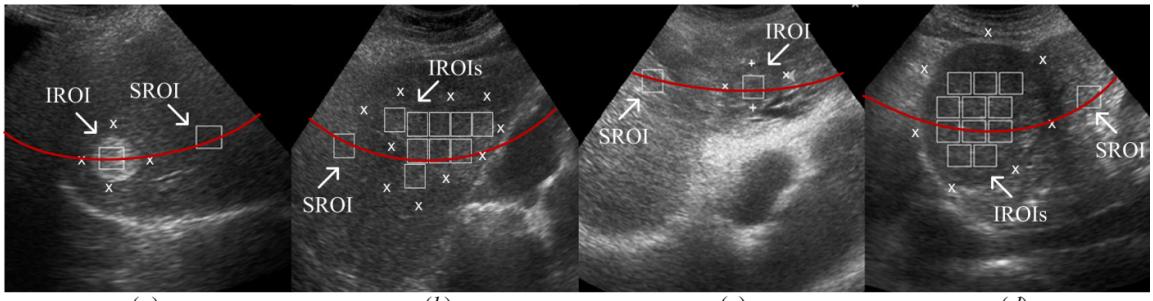

(*a*) (*b*) (*c*) (*d*)

Fig 3.2. Sample images with ROIs marked (*a*) typical HEM ; (*b*) atypical HEM ; (*c*) SHCC; (*d*) LHCC.
Note: SROI: Surrounding lesion ROI; IROI: Inside Lesion ROI; HEM: Hemangioma; SHCC: Small hepatocellular carcinoma; LHCC: Large hepatocellular carcinoma.

3.2.4 Selection of ROI size

The selection of ROI size is done carefully, considering the fact that it should provide adequate number of pixels for computing the texture properties. The different sized ROIs have been selected in the literature for the classification of FLLs such as, 10 × 10 pixels [54, 55], 32 × 32 pixels [2, 7, 8, 24], and 64 × 64 pixels [9]. In this research work, multiple ROIs of size 32 × 32 pixels are manually extracted from each lesion considering the facts given below:

(*a*) It has been shown in earlier studies that ROI size with 800 pixels or more provide good sampling distribution for estimating reliable statistics. The ROI size of 32 × 32 contains 1024 pixels and therefore, the texture features computed can be considered to be reliable estimates.

(*b*) The participating radiologists suggested avoiding larger sized ROIs because some lesions contain necrotic areas. Therefore, radiologists opined that necrotic area inside the lesions should be avoided during IROIs extraction. Further, the participating radiologists were of the view that SROI for every lesion should be chosen by avoiding inhomogeneous areas such as blood vessels and hepatic ducts etc., which is practically not possible by considering larger sized ROIs.

(*c*) The ROIs, which are smaller in size, takes less time for feature computation in comparison to the larger sized ROIs. Also, more number of samples is available by considering smaller sized ROIs.

3.3 Methods

3.3.1 Generalized CAD System Design

The CAD system is used to assist radiologists in the diagnosis of FLLs. The Generalized CAD system design is given in Fig. 3.3. The ROI extraction module is described in section 3.2.3 and 3.2.4. The feature extraction module is described in detail in section 5.4. The feature selection module is optional and therefore is not considered in the present work. A wide variety of classifiers are used for the classification task. The classifiers used to carry out the present research work are described in section 3.3.3.

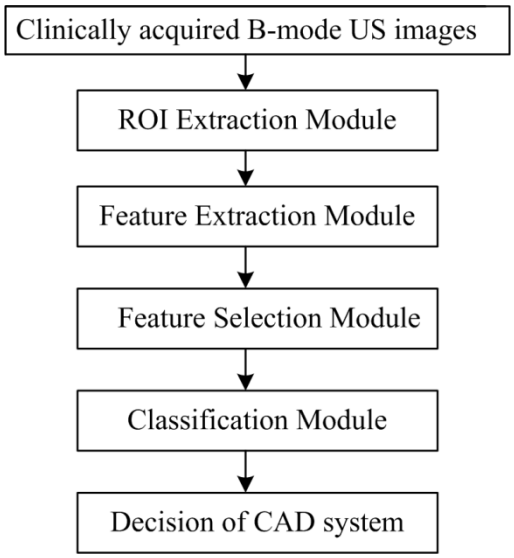

Fig. 3.3. Generalized CAD System Design.

3.3.2 Feature Extraction Module

The main idea behind feature extraction is to compute the mathematical descriptors describing the properties of ROI. These mathematical descriptors are further classified as shape based features and texture based features [59, 60]

The participating radiologists opined that the shape based features do not provide any significant information for differential diagnosis between HEM and HCC lesions. Accordingly, the proposed CAD system design is based on the textural features only. The texture feature extraction methods are generally classified into statistical, spectral and spatial filtering based methods. From the exhaustive review of the related studies on classification of FLLs [2, 7, 8, 9, 24, 54, 55], it can be observed that all these texture features are important for the classification of FLLs. Accordingly, for the present task of classification between HEM and HCC lesions, the texture features are extracted for each

ROI image using statistical, spectral and spatial filtering based methods as shown in Fig. 3.4.

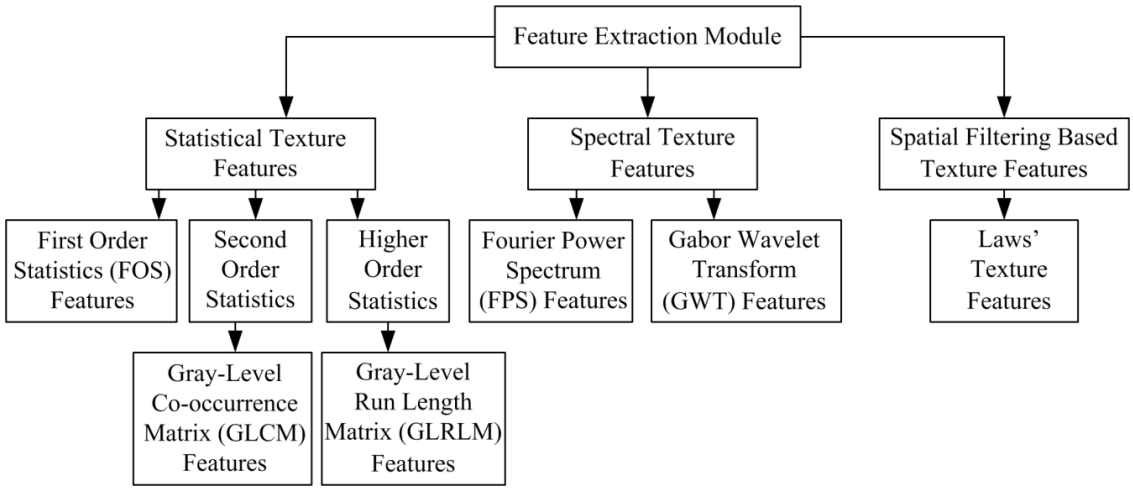

Fig. 3.4. Texture features computed for each ROI image.

3.3.3 Classification Module

The task of a classifier is to assign a given sample to its concerned class. Classification is a machine learning technique used to predict the class membership of unknown data instances based on the training set of data containing instances whose class membership is known. In this module different classifiers like SVM and SSVM are employed to classify the unknown testing instances of liver US images of different classes based on the training instances. To avoid any bias induced by unbalanced feature values the extracted features are normalized between 0 and 1, by using min-max normalization procedure.

3.3.3.1 Support Vector Machine (SVM) Classifier

The SVM classifier belongs to a class of supervised machine learning algorithms. It is based on the concept of decision planes that define the decision boundary. In SVM, kernel functions are used to map the non-linear training data from input space to a high dimensionality feature space.. The polynomial, Gaussian radial basis function and sigmoid kernel are used in general [61- 64]. In the present work, LibSVM library has been used for the implementation of SVM classifier [65] and the performance of the Gaussian radial basis kernel function has been examined. The optimal choice of kernel parameter γ and regularization parameter C is the crucial step in attaining good generalization performance. The regularization parameter C keeps low training error value and tries to maximize the margin while the kernel parameter γ decides the curvature of decision

boundary. In present work, 10-fold cross validation is carried out on training data for each combination of (C, γ), such that, $C \varepsilon \{2^{-4}, 2^{-3} \ldots 2^{15}\}$ and $\gamma \varepsilon \{2^{-12}, 2^{-11} \ldots 2^{4}\}$. The optimum values of C and γ can be obtained by this grid search procedure in the parameter space for which the training accuracy is maximum.

3.3.3.2 Smooth Support Vector Machine (SSVM) Classifier

To solve important mathematical problems related to programming, smoothing methods are extensively used. The SSVM works on the idea of smooth unconstrained optimization reformulation based on the traditional quadratic program which is associated with SVM [66, 67]. For implementing SSVM classifier, the SSVM toolbox [68] developed by Laboratory of Data Science and Machine Intelligence, Taiwan has been used. Similar to SVM implementation in case of SSVM also, 10-fold cross validation is carried out on training data for each combination of (C, γ), such that, $C \varepsilon \{2^{-4}, 2^{-3} \ldots 2^{15}\}$ and $\gamma \varepsilon \{2^{-12}, 2^{-11} \ldots 2^{4}\}$. The optimum values of C and γ can be obtained by this grid search procedure in the parameter space for which the training accuracy is maximum.

3.4 Concluding Remarks

It has been shown in earlier studies that ROI size with 800 pixels or more provide good sampling distribution for estimating reliable statistics. In the present work, the ROI size of 32 × 32 had been considered as it contains 1024 pixels and therefore, the texture features computed can be considered to be reliable estimates.

After carrying out extensive literature survey, it was observed that various CAD system designs have proven useful to the radiologists in routine medical practice as second opinion tools for classification of Liver US images in cases where a clear discrimination cannot be made subjectively between the overlapping sonographic appearances. In light of this fact, different CAD system designs employing the texture analysis techniques of feature extraction and feature classification have been proposed in the present work. Feature extraction is done using statistical, spectral and spatial filtering based methods.

A detailed description of the CAD system designs is given in the forthcoming chapters.

Chapter 4

Comparative analysis of Despeckle filters for Liver US images

4.1. Introduction

In the present work, a comprehensive image dataset consisting of B-mode liver US images of (*a*) NOR liver, (*b*) cirrhotic liver, (*c*) typical and atypical cases of Cyst, HEM, and MET lesions, and (*d*) SHCC and LHCC cases, is used for evaluation of despeckling algorithms. In the present study, ten despeckle filtering algorithms based on local statistics, non-linear filtering, and diffusion filtering, have been applied on the B-mode liver US images. The IQEMs has been computed for the performance evaluation of despeckle filtering techniques.

4.2. Despeckle Filtering

The US images can be pre-processed by using several despeckling techniques. In the present work, ten despeckling filters, which fall under the category of local statistics, non-linear filtering, and diffusion filtering, have been implemented on 151 B-mode liver US images as shown in Fig. 4.1.

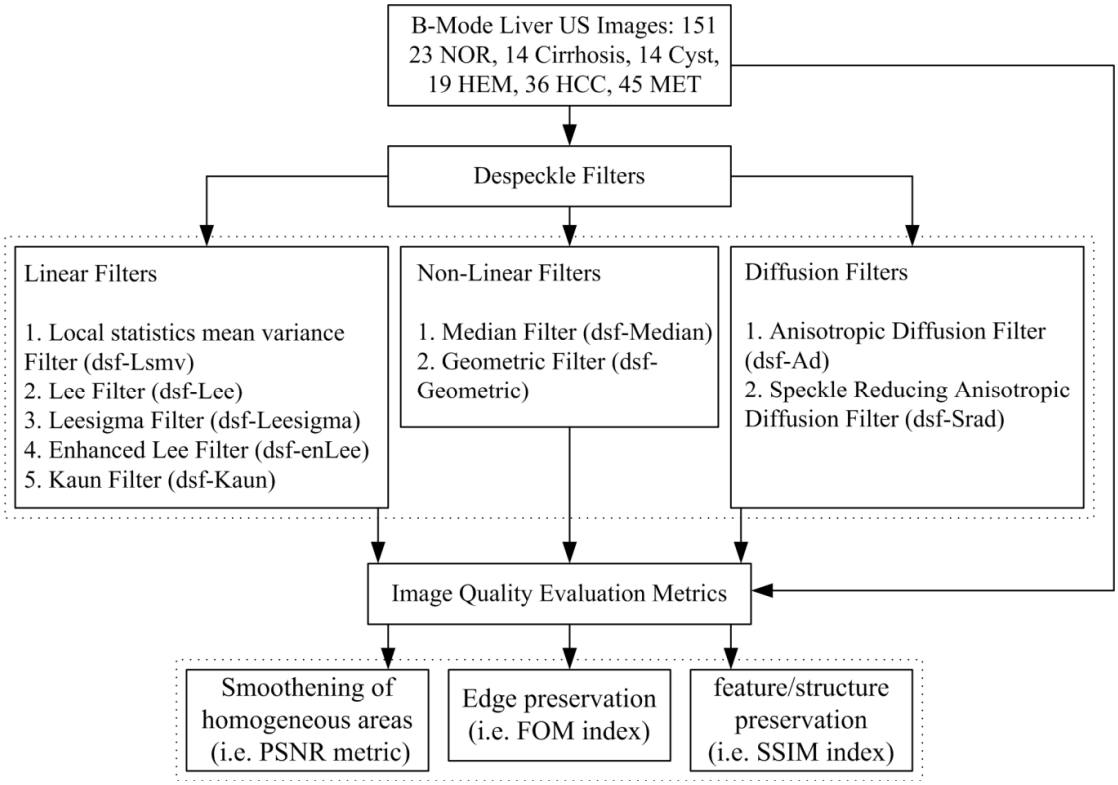

Fig. 4.1. Despeckle Filters and Image Quality Evaluation Metrics used for the present work.

4.2.1 Local Statistics Filters

4.2.1.1 dsf - Lsmv (despeckle filter - Local statistics mean variance)

In this algorithm, first order statistics i.e. mean and variance of the neighborhood is calculated to estimate the speckle free pixel given by the equation [36- 40]:

$$\hat{I}_{i,j} = \bar{n} + k_{i,j}\left(n_{i,j} - \bar{n}\right), \tag{1}$$

here, $\hat{I}_{i,j}$ represents the modified noise free pixel, $n_{i,j}$ represents the value of noisy pixel in the moving window (say, $N_1 \times N_2$), $\bar{n}$ is the estimated mean value in the moving window . The variable, $k_{i,j}$ serves as the weighting factor, with i, j acts as pixel coordinates and $k \in [0, 1]$. In the moving window, $k_{i,j}$ is the local statistics function and can be computed in various forms as given below:

$$k_{i,j} = (1 - \bar{n}^2\sigma^2)/\left(\sigma^2(1 + \sigma_n^2)\right), \tag{2}$$

$$k_{i,j} = \sigma^2/(\bar{n}^2\sigma_n^2 + \sigma^2), \tag{3}$$

$$k_{i,j} = (\sigma^2 - \sigma_n^2)/\sigma^2, \tag{4}$$

here, σ^2 represents the moving window variance while σ_n^2 is the noise variance in the original window. The noise variance can be obtained by:

$$\sigma_n^2 = \sum_{z=1}^{a} \sigma_z^2/\bar{n}_z, \tag{5}$$

here, $\bar{n}_z$ and σ_z^2 indicates the mean and variance of the noise in the chosen window, respectively. The variable, a, is the pointer covering every window in the complete image.

4.2.1.2 dsf - Lee (despeckle filter - Lee)

Lee [36, 37] filter depends on the multiplicative speckle model. The local statistics is used to conserve feature and edges efficiently. The smoothing is done over the area where the value of variance is low (e.g. homogeneous areas), while the areas with high variance (i.e. edges) remain intact. The enhanced value of pixel i, j in the moving window, $\hat{I}_{i,j}$ can be estimated as:

$$\hat{I}_{i,j} = \bar{I}_{i,j} + k_{i,j}\left(I_{i,j} - \bar{I}_{i,j}\right), \tag{6}$$

here, $\bar{I}_{i,j}$ represents the mean intensity value in the moving window, and $k_{i,j}$, the adaptive filter coefficient can be determined as:

$$k_{i,j} = Q_{i,j} - \left(Q_{i,j}/\sigma_1^2\right), \tag{7}$$

here, $Q_{i,j}$ is the *a priori* variance of the $I_{i,j}$ and σ_1 is the noise variance.

4.2.1.3 dsf - Leesigma (despeckle filter - Leesigma)

The Lee-sigma [41] filter smoothes the noisy image by averaging the intensities of those neighbour pixels which are present within the sigma range of the central pixel. It requires intensity range specifications and window size, N×M.

$$\hat{I}_{i,j} = \frac{\left(\sum_{z=i-N}^{N+i}\sum_{y=j-M}^{M+j}(\delta_{z,y}I_{z,y})\right)}{\left(\sum_{z=i-N}^{N+i}\sum_{y=j-M}^{M+j}(\delta_{z,y})\right)}, \tag{8}$$

$$\delta_{z,y} = 1, \text{ if } \left(I_{i,j} - \Delta\right) \leq I_{z,y} \leq \left(I_{i,j} + \Delta\right) \tag{9}$$

$$= 0, \text{otherwise.}$$

here, $\Delta = 2\sigma$.

4.2.1.4 dsf - enLee (despeckle filter – enhanced Lee)

The enhanced Lee [42] filter is the modified version of the Lee filter. This filter improves the edge preservation ability in the despeckled image. The filtering formula and the weighting function are as given below:

$$\hat{I} = \bar{I}, \qquad C_I \leq C_s \tag{10}$$

$$\hat{I} = I_{i,j}k_{i,j} + \bar{I}_{i,j}\left(1 - k_{i,j}\right), \quad C_s < C_I < C_{max} \tag{11}$$

$$\hat{I} = \bar{I}, \qquad C_I \geq C_{max} \tag{12}$$

$$k_{i,j} = \exp\{-k_d[(C_I(i,j) - C_s)/(C_{max} - C_I(i,j))]\}, \tag{13}$$

here, C_I is the image class which is to be averaged and filtered, C_s is the coefficient of variation, and k_d is the filter parameter.

4.2.1.5 dsf - Kaun (despeckle filter – Kaun)

The Kaun [43, 44] filter works on the local image statistics to suppress the speckle noise efficiently. For an ideal image, the filtering formula, $\hat{I}_{i,j}$, with intensity I, multiplicative noise model is:

$$\hat{I}_{i,j} = I_{i,j}k_{i,j} + \bar{I}_{i,j}\left(1 - k_{i,j}\right), \tag{14}$$

here, $k_{i,j}$ is the weighting function and can be calculated as:

$$k_{i,j} = [1 - C_u^2/C_I^2(i,j)]/[1 + C_u^2], \tag{15}$$

here, the noise variation coefficient, $C_u = \sigma_u / \bar{u}$.

4.2.1.6 dsf - Frost (despeckle filter – Frost)

The Frost [38] filter uses a rapidly changing convolution kernel that readjusts itself in areas containing the edges by applying local statistics. The filtering output can be determined as:

$$\hat{I}_{i,j} = \sum_{p \in \eta} m_p I_p, \tag{16}$$

here,

$$m_p = \exp\left(-KC_s^2 b_{s,p}\right) / \sum_{p \in \eta} \exp\left(-KC_s^2 b_{s,p}\right), \tag{17}$$

$$b_{s,p} = \sqrt{\left(i - i_p\right)^2 + \left(j - j_p\right)^2}, \tag{18}$$

here, K indicates the damping factor, (i, j) and (i_p, j_p) represents the coordinates of grid for pixel s and p, respectively. In homogeneous areas, K acts as the mean filter with its value approaches to zero, while at an edge the value of K becomes very large to keep the pixel unchanged.

4.2.2 Non-Linear Filters

4.2.2.1 dsf - Median (despeckle filter – Median)

The dsf - Median (despeckle filter - Median) [45] filter is used to reduce random noise and acts as a non-linear operator. When the median filtering is applying on the pixel $x_{i,j}$ with the moving window size M×N, the resulting pixel $y_{i,j}$ represents the median value of all the neighbor pixels present in that window.

$$\hat{I}_{i,j} = 2n + \left|\bar{d}\right| + 1.5 + 0.5p_0, \tag{19}$$

here, n × n is the window size and $\left|\bar{d}\right|$ is the average of absolute values of horizontal adjacent gray level difference of median filtered image. p_0 indicates the probability of d to be zero in an image.

4.2.2.2 dsf – GF (despeckle filter – Geometric)

The dsf - Gf (despeckle filter - Geometric) [46, 47] filter uses a linear noise reduction technique to gently decimate the bright and dark edges of the speckle noise, iteratively. It works on the 3×3 neighbourhood and compares the central pixel intensity with the

remaining pixels in window. The value of the intensity of the central pixel is changed according to the intensities of the eight neighbors to make it more representative than the surroundings. The dsf - Gf filter operation can be described with Fig. 4.2.

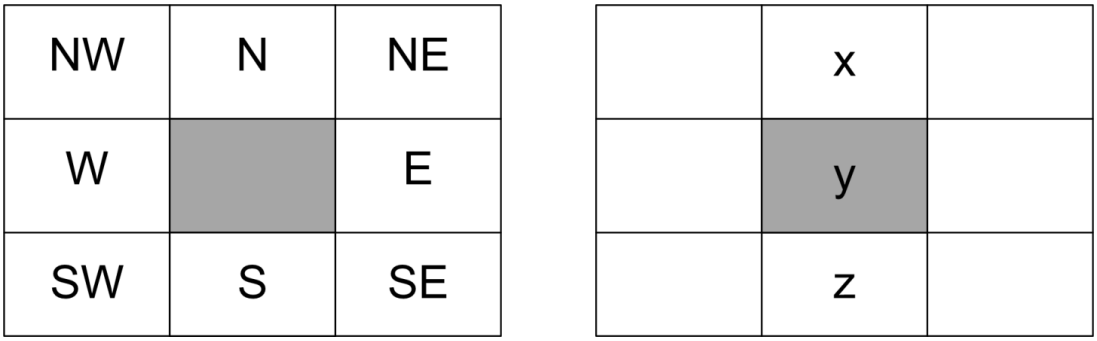

(*a*) (*b*)

Fig. 4.2. (*a*) Directions of implementation of geometric filter. (*b*) Pixels selected for the N-S direction (intensity of central pixel z is adjusted based on the values of intensities of pixel x, y, and z.

(i) Pixel value allocation: The x, y, and z pixels are selected in the north-south (NS) direction as shown in the Fig. 4.2 (a) and (b).

(ii) Central Pixel adjustment: The following adjustments in intensity value are done for the pixel y [see Fig. 4.2(b)]:

$$\text{if } x \geq y + 2 \text{ then } y = y + 1,$$
$$\text{if } x > y \text{ and } y \leq z \quad \text{then } y = y + 1,$$
$$\text{if } z > y \text{ and } y \leq x \text{ then } y = y + 1,$$
$$\text{if } z \geq y + 2 \text{ then } y = y + 1,$$
$$\text{if } x \geq y - 2 \text{ then } y = y - 1,$$
$$\text{if } x < y \text{ and } y \geq z \text{ then } y = y - 1,$$
$$\text{if } z < y \text{ and } y \geq x \text{ then } y = y - 1,$$
$$\text{if } z \geq y - 2 \text{ then } y = y - 1.$$

(iii) Repeat: Repeat the above steps for the east-west (EW) direction, north-west to south-east (NW-SE) direction, and south-west to north-east (SW-NE) direction [see Figure 4.2(a)].

4.2.3 Diffusion Based Filters

4.2.3.1 dsf - Ad (despeckle filter – Anisotropic Diffusion)

The anisotropic diffusion [38, 48- 52] simultaneously performs the noise reduction and contrast enhancement. It is a non-linear technique which smoothes the homogeneous areas and retains the edges, therefore applies directly on the logarithmically compressed images.

$$\begin{cases} \frac{\partial u(i,j;t)}{\partial t} = \nabla[c(|\nabla I_\sigma(i,j;t)|).\nabla I(i,j;t)) \\ I(i,j;0) = I_0(i,j) \end{cases} \quad (20)$$

here, $\nabla I(i,j;t)$ represents the original image. $\partial I(i,j;t)/\partial t$ indicates the partial derivation of $I(i,j;t)$.

4.2.3.2 dsf - Srad (despeckle filter – Speckle Reducing Anisotropic Diffusion)

The speckle reducing anisotropic diffusion [51 filter is an edge sensitive diffusion method for speckled images. It applies the coefficient of variation and process the direct data to preserve the important details in the image. The coefficient of variation can be computed as:

$$z(i,j;t) = \frac{std[I(i,j;t)]}{\bar{I}(i,j;t)}, \quad (21)$$

$$c[z(i,j;t), z_0(t)] = \left(1 + \frac{z^2(i,j;t) - z_0(t)}{z^2(i,j;t)(1+z_0^2(t))}\right), \quad (22)$$

here, $z(i,j;t)$ gives the ratio of standard deviation to mean and z_0 represents the speckle scale function.

4.3 Despeckle Filtering: Performance Parameters

The ten despeckle filtering algorithms has been applied on all the 151 images, pre-processed by different despeckled filters, along with the original image. The IQEMs, which includes, (a) PSNR metric (for smoothening of homogeneous areas), (b) FOM index (for edge preservation), and (c) SSIM index (for feature/structure preservation), have been computed for the pre-processed images. These indices, which indicate the different performance measures, are shown in Table 4.1. The below mentioned image quality metrics, depend on mutual information between the original and despeckled images and their natural scene statistics, has recently been used by Gupta *et al.* [53].

Here, $I_{i,j}$ is the original image and $I'_{i,j}$ represents the despeckled image. The intensity of original image is indicated using I^2_{max}. The value of PSNR is comparatively low for poor despeckled images and higher for good despeckled images. In case of SSIM, c_1 = 0.01d and c_2 = 0.03d, with d= 255 represents dynamic range of the US images. The SSIM range of values lies within 1 for the finest alikeness and -1 for the worst alikeness between the original image and despeckled image. For FOM, u_I and $u_{I'}$ represents the number of detected edge points in the original and the despeckled images, respectively. The positive

scaling factor is indicated by γ shows and d_i indicates the deviation or error from the ith detected edge pixel.

Table 4.1. IQEMs for 151 liver US images.

IQEMs	INVESTIGATOR	INDEX	FORMULA
PSNR	[32]	Speckle Reduction	$-20\log_{10}\left(\frac{\frac{1}{RC}\sum_{i=1}^{R}\sum_{j=1}^{C}\left(I_{i,j}-I'_{i,j}\right)^2}{I_{max}^2}\right)$
FOM	[33, 34]	Edge Preservation	$\frac{1}{\max(u_I, u_{I'})}\left(\sum_{i=1}^{u_I}\frac{1}{1+\gamma d_i^2}\right)$
SSIM	[35]	Feature/ Structure Preservation	$\frac{(2\bar{I}\bar{I'}+c_1)(2\sigma_{II'}+c_2)}{\left(\bar{I}^2+\bar{I'}^2+c_1\right)\left(\sigma_I^2+\sigma_{I'}^2+c_2\right)}$

Note: IQEMs: Image Quality Evaluation Metrics; PSNR: Peak Signal to Noise Ratio; FOM: Figure of Merit; SSIM: Structural Similarity Index.

4.4 Results

The despeckled images of different Liver classes (i.e. NOR, Cirrhosis, Cyst, HEM, HCC, and MET) of liver are shown in Fig. 4.3 to Fig. 4.8. The performance of the filters has been analysed for different performance parameters including speckle reduction, edge preservation and feature/structure preservation. The IQEMs for 23 NOR, 14 Cirrhosis, 14 Cyst, 19 HEM (typical and atypical), 36 HCC (SHCC and LHCC), and 45 MET (typical and atypical) cases of B-mode liver US images are tabulated in Table 4.2 in the form of mean SD standard deviation (μ SD s.d.). Among all the ten despeckle filtering algorithms implemented in the present work, the despeckle filter – Leesig yields the best performance with highest value for noise reduction capability (i.e. highest PSNR), highest value for edge preservation capability (i.e. highest FOM) and highest value for feature/structure preservation capability (i.e. highest SSIM) for all US liver images classes.

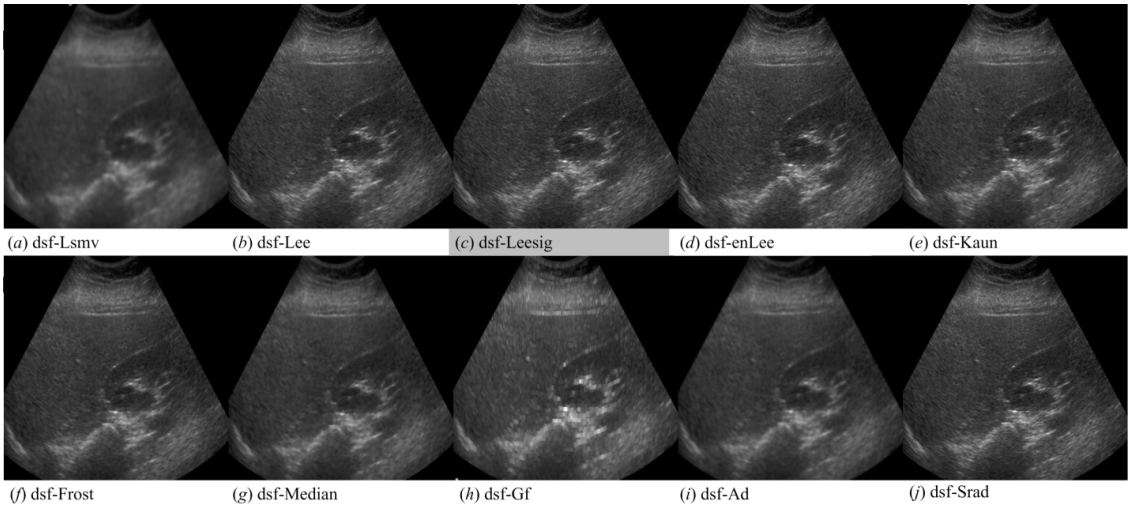

Fig. 4.3. The images of NOR liver despeckled by different filters. The dsf-Leesig filter yielding the best result is shaded with gray background.

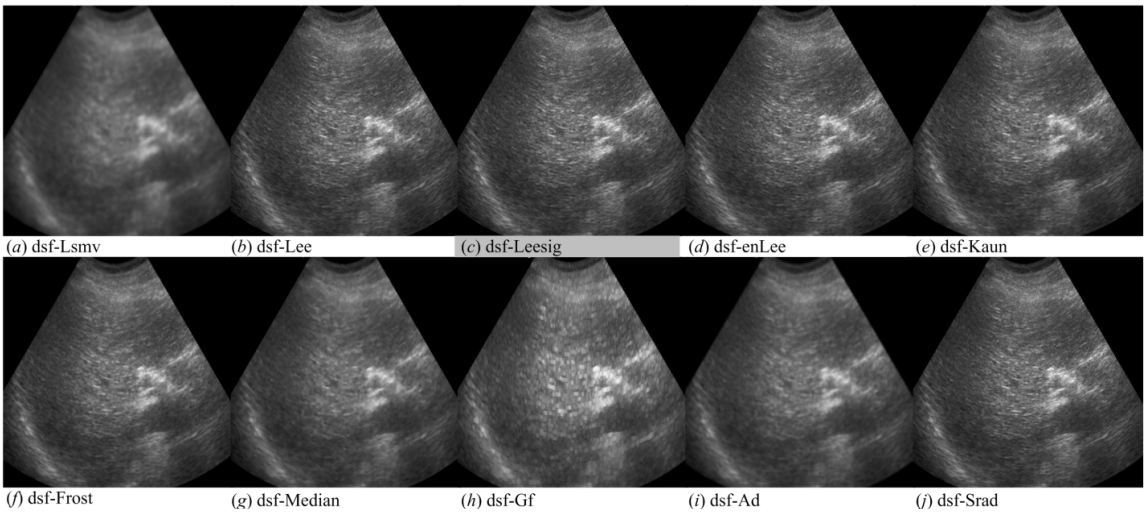

Fig. 4.4. The images of Cirrhotic liver despeckled by different filters. The dsf-Leesig filter yielding the best result is shaded with gray background.

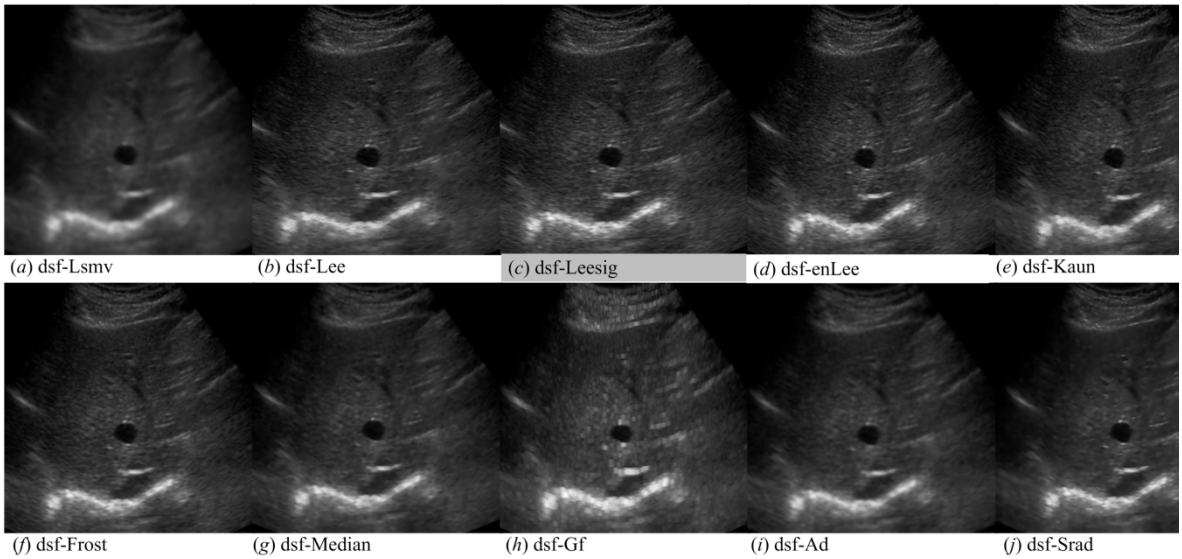

Fig. 4.5. The images of typical Cyst despeckled by different filters. The dsf-Leesig filter yielding the best result is shaded with gray background.

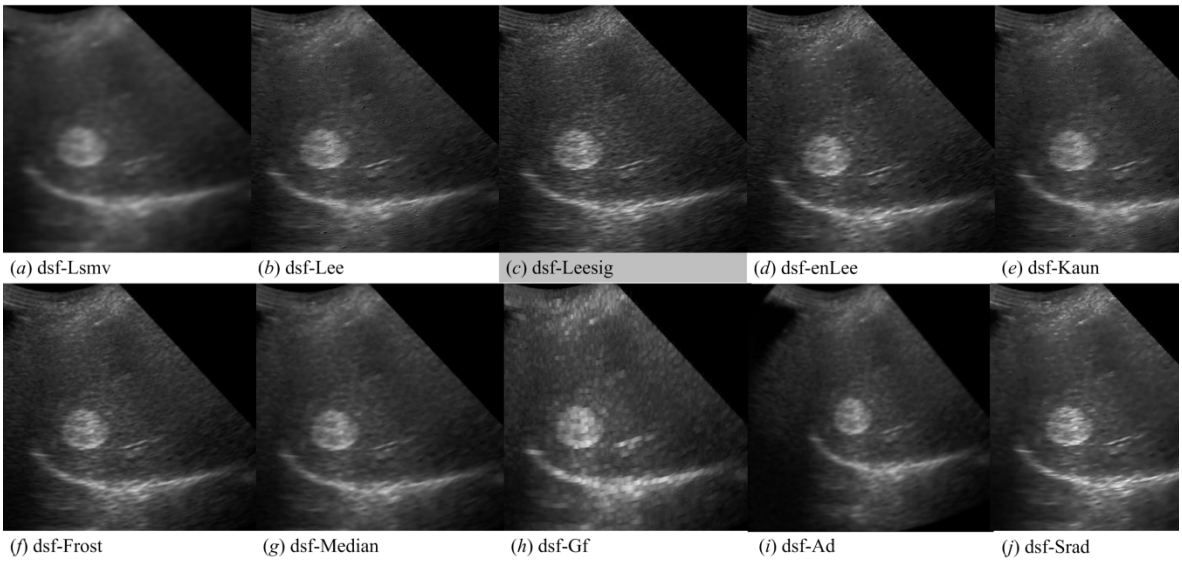

Fig. 4.6. The images of typical HEM despeckled by different filters. The dsf-Leesig filter yielding the best result.

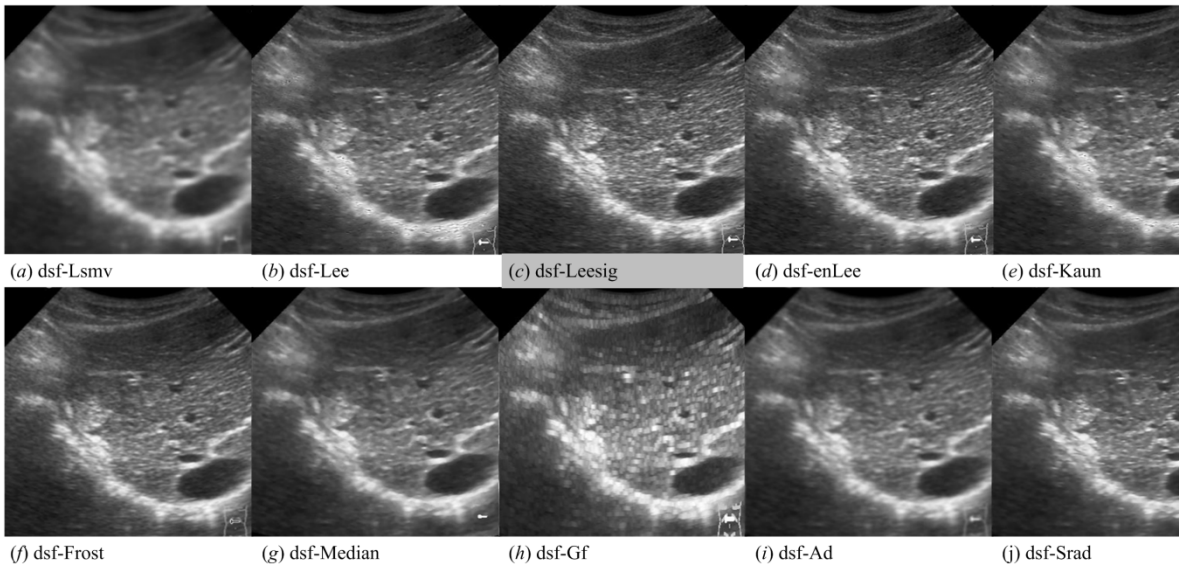

Fig. 4.7. The images of SHCC despeckled by different filters. The dsf-Leesig filter yielding the best result is shaded with gray background.

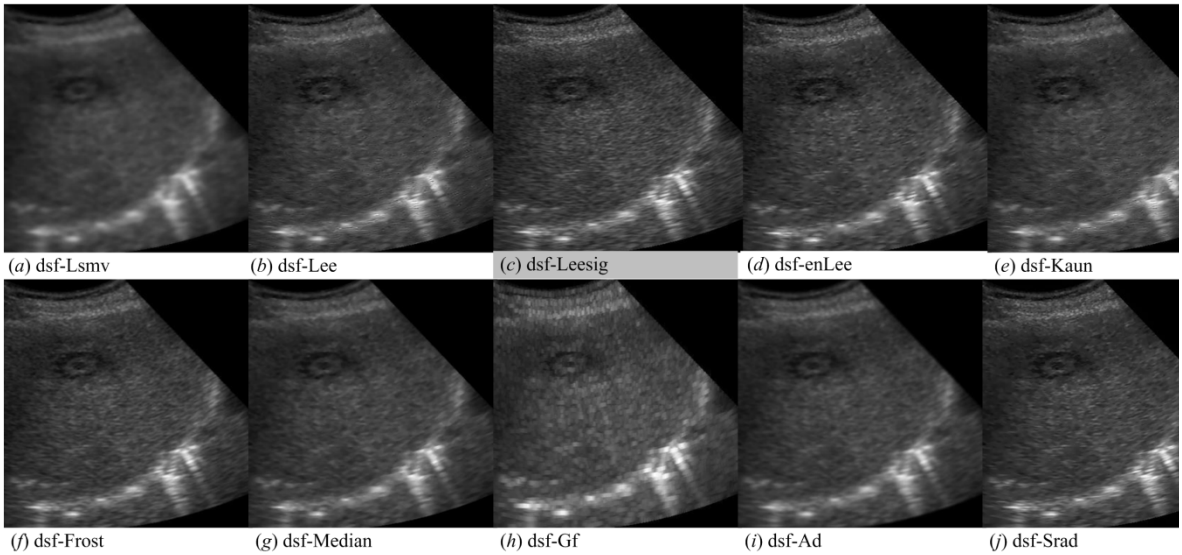

Fig. 4.8. The images of typical MET despeckled by different filters. The dsf-Leesig filter yielding the best result is shaded with gray background.

Table 4.2. IMAGE QUALITY EVALUATION METRICS (IQEMs) computed for 151 liver US images.

IQEMs for 23 NOR images					
IQEMs	**dsf-Lsmv**	**dsf-Lee**	**dsf-Leesig**	**dsf-enLee**	**dsf-Kaun**
PSNR	27.897 SD 0.97	34.417 SD 0.10	*34.505 SD 0.02*	19.372 SD 0.24	34.418 SD 0.10
FOM	0.5881 SD 0.05	0.9698 SD 0.02	*0.9839 SD 0.02*	0.8278 SD 0.01	0.9699 SD 0.02
SSIM	0.8748 SD 0.01	0.8965 SD 0.01	*0.8976 SD 0.01*	0.6586 SD 0.02	0.8965 SD 0.01
IQEM	**dsf-Frost**	**dsf-Median**	**dsf-Gf**	**dsf-Ad**	**dsf-Srad**
PSNR	27.225 SD 0.19	22.682 SD 0.18	19.201 SD 0.28	14.303 SD 1.22	14.306 SD 1.22
FOM	0.9202 SD 0.01	0.7843 SD 0.02	0.7661 SD 0.02	0.7833 SD 0.04	0.7615 SD 0.05
SSIM	0.8711 SD 0.01	0.8547 SD 0.01	0.7501 SD 0.01	0.3213 SD 0.01	0.3213 SD 0.01
IQEMs for 14 Cirrhosis images					
IQEMs	**dsf-Lsmv**	**dsf-Lee**	**dsf-Leesig**	**dsf-enLee**	**dsf-Kaun**
PSNR	26.809 SD 0.57	34.524 SD 0.11	34.553 SD 0.13	34.524 SD 0.11	34.524 SD 0.11
FOM	0.6284 SD 0.05	0.9779 SD 0.02	0.9838 SD 0.02	0.8224 SD 0.02	0.9780 SD 0.02
SSIM	0.8702 SD 0.02	0.8974 SD 0.01	0.8977 SD 0.01	0.6642 SD 0.03	0.8974 SD 0.01
IQEMs	**dsf-Frost**	**dsf-Median**	**dsf-Gf**	**dsf-Ad**	**dsf-Srad**
PSNR	27.021 SD 0.32	22.541 SD 0.43	19.105 SD 0.39	13.391 SD 0.85	13.394 SD 0.85
FOM	0.9222 SD 0.01	0.7815 SD 0.02	0.7679 SD 0.03	0.7963 SD 0.04	0.8053 SD 0.05
SSIM	0.8690 SD 0.01	0.8485 SD 0.02	0.7585 SD 0.02	0.3486 SD 0.03	0.3486 SD 0.03
IQEMs for 14 Cyst images					
IQEMs	**dsf-Lsmv**	**dsf-Lee**	**dsf-Leesig**	**dsf-enLee**	**dsf-Kaun**
PSNR	27.535 SD 0.75	34.895 SD 0.67	35.758 SD 0.07	19.470 SD 0.25	34.907 SD 0.65
FOM	0.6376 SD 0.05	0.9382 SD 0.02	0.9634 SD 0.02	0.8307 SD 0.01	0.9386 SD 0.02
SSIM	0.8882 SD 0.02	0.8975 SD 0.01	0.9057 SD 0.01	0.6961 SD 0.03	0.8976 SD 0.01
IQEMs	**dsf-Frost**	**dsf-Median**	**dsf-Gf**	**dsf-Ad**	**dsf-Srad**
PSNR	28.160 SD 0.23	22.903 SD 0.22	19.123 SD 0.25	15.141 SD 1.20	15.145 SD 1.20
FOM	0.9294 SD 0.02	0.8099 SD 0.03	0.7826 SD 0.02	0.8238 SD 0.03	0.7971 SD 0.05
SSIM	0.8842 SD 0.01	0.8691 SD 0.01	0.7738 SD 0.02	0.3651 SD 0.04	0.3651 SD 0.04
IQEMs for 19 HEM images					
IQEMs	**dsf-Lsmv**	**dsf-Lee**	**dsf-Leesig**	**dsf-enLee**	**dsf-Kaun**
PSNR	30.329 SD 0.99	31.930 SD 1.66	60.324 SD 7.01	25.650 SD 1.78	32.117 SD 1.60
FOM	0.5964 SD 0.04	0.8767 SD 0.03	0.9861 SD 0.01	0.8111 SD 0.01	0.8775 SD 0.03
SSIM	0.8089 SD 0.03	0.8851 SD 0.03	0.9925 SD 0.02	0.6409 SD 0.04	0.8895 SD 0.02
IQEMs	**dsf-Frost**	**dsf-Median**	**dsf-Gf**	**dsf-Ad**	**dsf-Srad**
PSNR	36.623 SD 2.39	32.236 SD 2.57	23.991 SD 1.44	14.717 SD 1.19	14.720 SD 1.20
FOM	0.9251 SD 0.01	0.8250 SD 0.03	0.7734 SD 0.01	0.8010 SD 0.03	0.8032 SD 0.04
SSIM	0.9687 SD 0.02	0.9059 SD 0.02	0.7163 SD 0.03	0.2144 SD 0.05	0.2146 SD 0.05
IQEMs for 36 HCC images					
IQEMs	**dsf-Lsmv**	**dsf-Lee**	**dsf-Leesig**	**dsf-enLee**	**dsf-Kaun**
PSNR	26.744 SD 1.39	31.709 SD 3.95	32.128 SD 4.13	18.732 SD 0.91	31.714 SD 3.95
FOM	0.6103 SD 0.04	0.9602 SD 0.03	0.9725 SD 0.02	0.8157 SD 0.02	0.9604 SD 0.03
SSIM	0.8857 SD 0.03	0.8969 SD 0.07	0.9020 SD 0.07	0.7037 SD 0.07	0.8970 SD 0.07
IQEMs	**dsf-Frost**	**dsf-Median**	**dsf-Gf**	**dsf-Ad**	**dsf-Srad**
PSNR	26.280 SD 1.48	22.322 SD 0.69	18.739 SD 0.72	13.447 SD 2.10	13.451 SD 2.10
FOM	0.9214 SD 0.02	0.7899 SD 0.04	0.7786 SD 0.02	0.8055 SD 0.04	0.8197 SD 0.06
SSIM	0.8808 SD 0.07	0.8811 SD 0.05	0.7786 SD 0.04	0.3462 SD 0.08	0.3463 SD 0.08
IQEMs for 45 MET images					
IQEMs	**dsf-Lsmv**	**dsf-Lee**	**dsf-Leesig**	**dsf-enLee**	**dsf-Kaun**
PSNR	30.046 SD 1.32	31.159 SD 1.34	60.346 SD 4.97	25.663 SD 1.37	31.345 SD 1.32
FOM	0.5750 SD 0.05	0.8614 SD 0.02	0.9864 SD 0.02	0.8050 SD 0.01	0.8635 SD 0.02
SSIM	0.7991 SD 0.03	0.8754 SD 0.04	0.9937 SD 0.03	0.6342 SD 0.05	0.8800 SD 0.04
IQEMs	**dsf-Frost**	**dsf-Median**	**dsf-Gf**	**dsf-Ad**	**dsf-Srad**
PSNR	36.924 SD 1.77	32.675 SD 1.52	23.895 SD 1.30	13.898 SD 1.42	13.900 SD 1.42
FOM	0.9240 SD 0.02	0.8354 SD 0.03	0.7669 SD 0.02	0.7956 SD 0.03	0.7992 SD 0.05
SSIM	0.9698 SD 0.03	0.9096 SD 0.02	0.7073 SD 0.03	0.1901 SD 0.04	0.1904 SD 0.04

Note: IQEMs: Image Quality Evaluation Metrics; PSNR: Peak Signal to Noise Ratio; FOM: Figure of Merit. SSIM: Structural Similarity Index. The values are represented in the form of μ SD s.d. The best performance is obtained by dsf-Leesig (shaded with gray background).

4.5 Concluding Remarks

In the present work, ten despeckle filtering algorithms have been implemented on a diversified data set of 151 conventional gray scale B-Mode liver US images for the speckle noise reduction as well as preservation of edges and features/ structures in the image, thereby, conserving the diagnostic information. From exhaustive objective (quantitative) analysis carried out in the present work, it can be concluded that Lee-sigma statistical despeckle filtering algorithm is ideally suited for despeckle filtering of B-Mode liver ultrasound images.

Chapter 5

CAD System Design for Classification of Primary benign and Primary malignant FLLs

5.1. Introduction

The aim of the present study is to develop a CAD system for differential diagnosis between HEM (i.e., primary benign FLL) and HCC (i.e., primary malignant FLL). The motivation behind considering these image classes is that the incidence of these lesions is very high in comparison to other primary benign and primary malignant lesions. Among the primary malignant lesions, hepatoblastoma (7%), cholangiocarcinoma and cystadenocarcinoma (6%) occur rarely therefore, the most commonly occurring primary malignant lesion i.e., HCC is considered [16- 18]. Among all the primary benign lesions of liver, HEM is the most commonly occurring primary benign FLL [1, 2, 3]. The differentiation between typical HEM and HCC is easy due to the typical sonographic appearance of the former one, but differential diagnosis between atypical HEM and HCC lesions is difficult even for the experienced radiologists [1].

In order to design an efficient classifier, it should be ensured that the database for designing the classifier should be diversified and comprehensive i.e., it should include both typical and atypical HEMs as well as SHCC and LHCC cases. Accordingly, the dataset used in the present work includes 10 typical and 6 atypical HEM images and 13 SHCCs and 15 LHCCs images.

The differential diagnosis between HEM and HCC lesions with the help of conventional gray scale B-mode US is considered difficult because of various limitations including: (*a*) limited sensitivity for the detection of SHCCs developed on the cirrhotic liver which is generally coarse-textured and nodular [1, 10, 11, 14, 19] , (*b*) in most of the cases, the sonographic appearances of HCC and atypical HEMs are overlapping [1, 10, 11, 19], (*c*) in certain cases , it is difficult to differentiate isoechoic lesions with very slim liver to lesion contrast [1, 12]. So, it is very important to overcome these limitations by design of an efficient CAD system with representative and diversified image database containing typical and atypical cases of HEM image class and SHCC and LHCC variants of the HCC image class.

As HCC develops on cirrhotic and nodular background, therefore, the experienced radiologists carry out differential diagnosis between atypical HEM and HCC by visual analysis of texture information of regions inside and outside the lesions. Therefore, in the present work, an investigation of contribution made by texture information present in the regions inside and outside of the lesion has been carried out for characterization of HEM and HCC lesions. For the classification task, SVM and SSVM classifier have been used [60- 64, 66, 67].

5.2. Data Set Description

In the present work, clinically acquired image database of 44 B-mode liver US images consisting of 16 HEM images with 16 solitary HEM lesions (i.e., 10 typical HEM lesions and 6 atypical HEM lesions) and 28 HCC images with 28 solitary HCC lesions (i.e., 13 SHCCs lesions and 15 LHCCs lesions) have been used. The description of the image database is given in Table 5.1.

Table 5.1. Description of image Database.

Clinically acquired B-mode liver US images (44) Total IROIs: 160, Total SROIs: 44		
	HEM	**HCC**
Total Images	16 Typical HEM: 10 Atypical HEM: 6	28 SHCC: 13 LHCC: 15
Total Lesions	16	28
Total IROIs	70 Typical HEM IROIs: 27 Atypical HEM IROIs: 43	90 SHCC IROIs: 19 LHCC IROIs: 71
Total SROIs	16	28

Note: SHCC: Small Hepatocellular Carcinoma (size varies from 1.5 to 1.9 cm); LHCC: Large Hepatocellular Carcinoma (size varies from 2.1 to 5.6 cm). IROIs: Inside ROIs, SROIs: Surrounding ROIs.

The final database comprising of total 160 IROIs and 44 SROIs was stored in Intel® Core™ I3-M 370, 2.40 GHz with 3 GB RAM.

In order to design an efficient classifier, it should be ensured that the training data should include representative cases from both the image sub-classes i.e., typical and atypical HEMs and SHCC as well as LHCC cases. Each image class was divided into two sets of images (training and testing set). To avoid biasing, the training ROIs were taken from the first set while testing ROIs were taken from the other set. The brief description of training and testing dataset is given in Table 5.2.

Table 5.2. Description of training and testing Dataset.

Description : Training dataset		
	HEM	**HCC**
Total images (26)	10	16
Total lesions	10 Typical HEM lesions: 7 Atypical HEM lesions: 3	16 SHCC lesions: 7 LHCC lesions: 9
Total IROIs (90)	40 Typical HEM IROIs: 22 Atypical HEM IROIs: 18	50 SHCC IROIs: 10 LHCC IROIs: 40
Total SROIs (26)	10	16
Description : Testing dataset		
Total images (18)	6	12
Total lesions	6 Typical HEM lesions: 3 Atypical HEM lesions: 3	12 SHCC lesions: 7 LHCC lesions: 9
Total IROIs (90)	40 Typical HEM IROIs: 22 Atypical HEM IROIs: 18	50 SHCC IROIs: 10 LHCC IROIs: 40
Total SROIs (26)	10	16

5.3. Proposed CAD System Design

For In the present work, the CAD system for characterization of HEM and HCC lesions using B-Mode US images has been proposed. The block diagram of the proposed CAD system design is shown in Fig. 5.1.

For implementing proposed CAD system design, the dataset of 160 non-overlapping IROIs and 44 SROIs was extracted from 44 clinically acquired B-mode liver US liver images. The CAD system includes feature extraction and classification modules. In feature extraction module, texture features are computed from 160 IROIs and 44 SROIs using FOS, second order statistics which includes GLCM method, higher order statistics i.e., GLRLM method, spectral features such as FPS and GWT features and spatial filtering based Laws' texture features. The texture feature set of 172 texture features containing 86 texture IROI features and 86 texture ratio features is considered for analysis. The feature set is further divided into training dataset and testing dataset. The bifurcation of ROIs of particular class in training and testing dataset is described in Table 5.2.

In classification module, two different classifiers, i.e., SVM and SSVM have been used for the classification task.

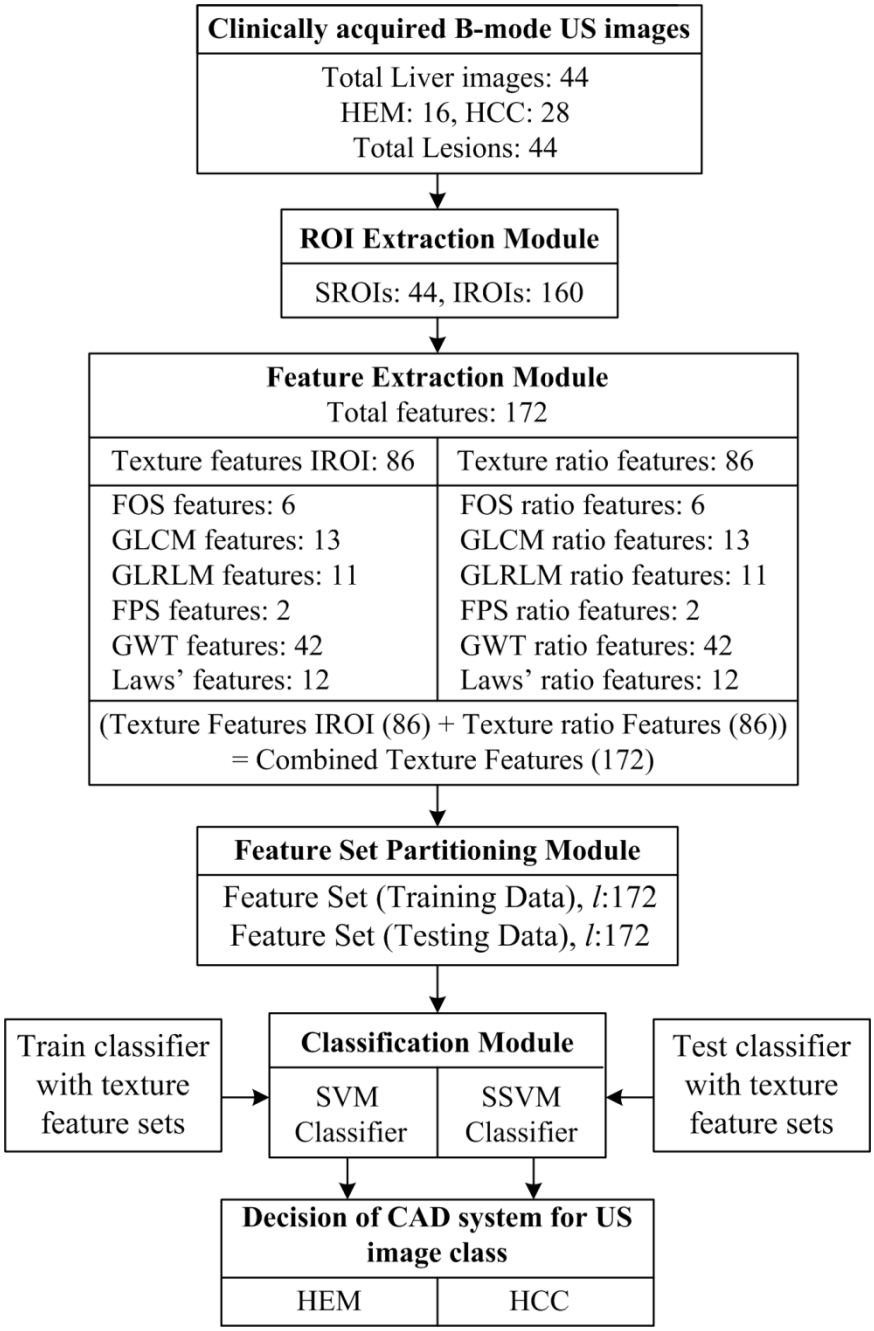

Fig. 5.1. Block diagram of proposed CAD system design
Note: *l*: Length of feature set.

5.4. Feature Extraction Module

The main idea behind feature extraction is to compute the mathematical descriptors describing the properties of ROI. These mathematical descriptors are further classified as shape based features and texture based features [59, 60].

The participating radiologists opined that the shape based features do not provide any significant information for differential diagnosis between HEM and HCC lesions.

Accordingly, the proposed CAD system design is based on the textural features only. The texture feature extraction methods are generally classified into statistical, spectral and spatial filtering based methods. From the exhaustive review of the related studies on classification of FLLs [2, 7, 8, 9, 24, 54, 55], it can be observed that all these texture features are important for the classification of FLLs. Accordingly, for the present task of classification between HEM and HCC lesions, the texture features are extracted for each ROI image using statistical, spectral and spatial filtering based methods as shown in Figure 5.2.

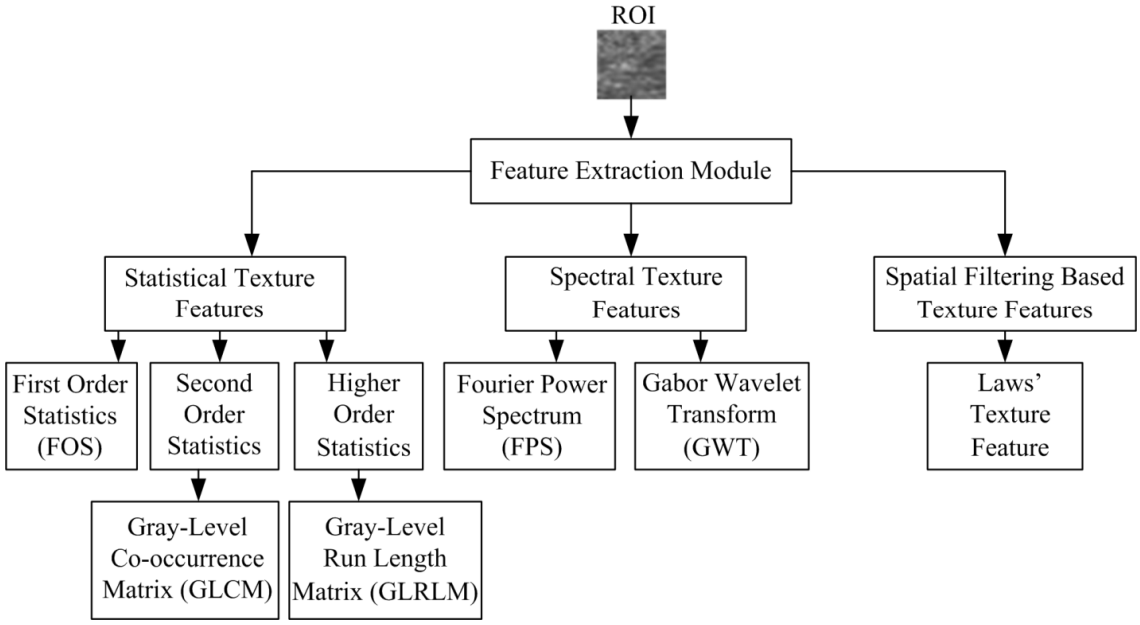

Fig. 5.2. Texture features computed for each ROI image.

In the present work, a total of 172 texture features (shown in Table 5.3) were computed by using statistical, spectral and spatial filtering based texture feature extraction methods. Further, these features are applied to the CAD system with a tedious task of joining all the effective features together. The brief description of these texture features is depicted below.

5.4.1 Statistical Texture Features (F1- F30)

The statistical texture features are based on spatial distribution of the gray level intensity values in image. The statistical feature extraction methods can be categorized as first order statistics (FOS), second order statistics (GLCM), and higher order statistics (GLRLM) based methods.

(*a*) FOS features (F1- F6): For each ROI, six textural features are computed with FOS method i.e., average gray level, smoothness, standard deviation, entropy, third moment and uniformity [2, 8, 23].

(*b*) GLCM features (F7- F19): For each ROI, thirteen textural features are computed with GLCM method i.e., contrast, angular second moment, inverse difference moment, correlation, sum average, variance, sum variance, difference variance, entropy, sum entropy, difference entropy, information measure of correlation-1 and information measure of correlation-2 [2, 8, 19, 69] .

Table 5.3. Description of 172 texture features extracted for characterization of HEM and HCC lesions.

Methods	**Features Description**		
Statistical	**FOS** (F1-F6)	**GLCM** (F7-F19)	**GLRLM** (F20-F30)
	F1: average gray level	F7: angular second moment	F20: short run emphasis
	F2: standard deviation	F8: contrast	F21: long run emphasis
	F3: smoothness	F9: correlation	F22: low gray level run emphasis
	F4: third moment	F10: sum of squares variance	F23: high gray level run emphasis
	F5: uniformity	F11: inverse difference moment	F24: short run low gray level emphasis
	F6: entropy	F12: information measures of correlation- 1	F25: short run high gray level emphasis
		F13: information measures of correlation- 2	F26: long run low gray level emphasis
		F14: sum entropy	F27: long run high gray level emphasis
		F15: entropy	F28: gray level non uniformity
		F16: difference variance	F29: run length non uniformity
		F17: difference entropy	F30: run percentage
		F18: sum average	
		F19: sum variance	
Spectral	**FPS** (F31-F32)	**GWT** (F33-F74)	
	F31: angular sum	*F33- F53: mean	
	F32: radial sum	*F54- F74: standard deviation	
Spatial Filtering	**Laws'** (F75-F86)		
	F75: $LL_{(mean)}$	F79: $LS_{(mean)}$	F83: $SS_{(std)}$
	F76: $EE_{(mean)}$	F80: $ES_{(mean)}$	F84: $LE_{(std)}$
	F77: $SS_{(mean)}$	F81: $LL_{(std)}$	F85: $LS_{(std)}$
	F78: $LE_{(mean)}$	F82: $EE_{(std)}$	F86:$ES_{(std)}$

Note: F87-F172: 86 texture ratio features corresponding to above features (F1-F86). Features F1to F86 are computed for each IROI and SROI so as to compute another 86 texture ratio features (F87-F172) corresponding to the above features. *(F33- F74) two statistical parameters computed out of 21 feature images obtained as a result of convolving 21 Gabor filters with each ROI image. These 21 wavelet filters were computed by considering 3 scales (0, 1, 2) and 7 orientations (22.5°, 45°, 67.5°, 90°, 112.5°, 135°,157.5°).

(*c*) GLRLM features (F20- F30): For each ROI, eleven textural features are computed with GLRLM method i.e., long run emphasis (LRE), short run emphasis (SRE), high gray level run emphasis (HGLRE), low gray level run emphasis (LGLRE), short run high gray level emphasis (SRHGLE), short run low gray level emphasis (SRLGLE), long run high

gray level emphasis (LRHGLE), long run low gray level emphasis (LRLGLE), gray level non-uniformity (GLN), run length non-uniformity (RLN) and run percentage (RP) [2, 8, 63, 70- 72].

5.4.2 Spectral Texture Features (F31- F74)

The spectral texture features can be computed by FPS method and GWT method as described below:

(*a*) FPS features (F31- F32): For each ROI, two features i.e., angular sum and radial sum of the discrete Fourier transform (i.e., DFT) has been computed using FPS method [2, 70].

(*b*) GWT features (F33- F74): Gabor filter provides useful texture descriptors by using multi-scale features estimated at different scales and orientations. The 2D-GWT, considering three scales (0, 1, 2) and seven orientations (22.5°, 45°, 67.5°, 90°, 112.5°, 135°, 157.5°), result in a group of (7 × 3 = 21) wavelets. When this group of Gabor filters family of 21 wavelets is convolved with a given ROI image, a set of 21 feature images are obtained. The real parts of Gabor filter family of twenty one feature images obtained for a sample HEM ROI image is shown in Fig. 5.3. From these 21 feature images, mean and standard deviation are computed as texture descriptors resulting in (21 feature images × 2 statistical parameters = 42) features for each ROI [25, 60, 73].

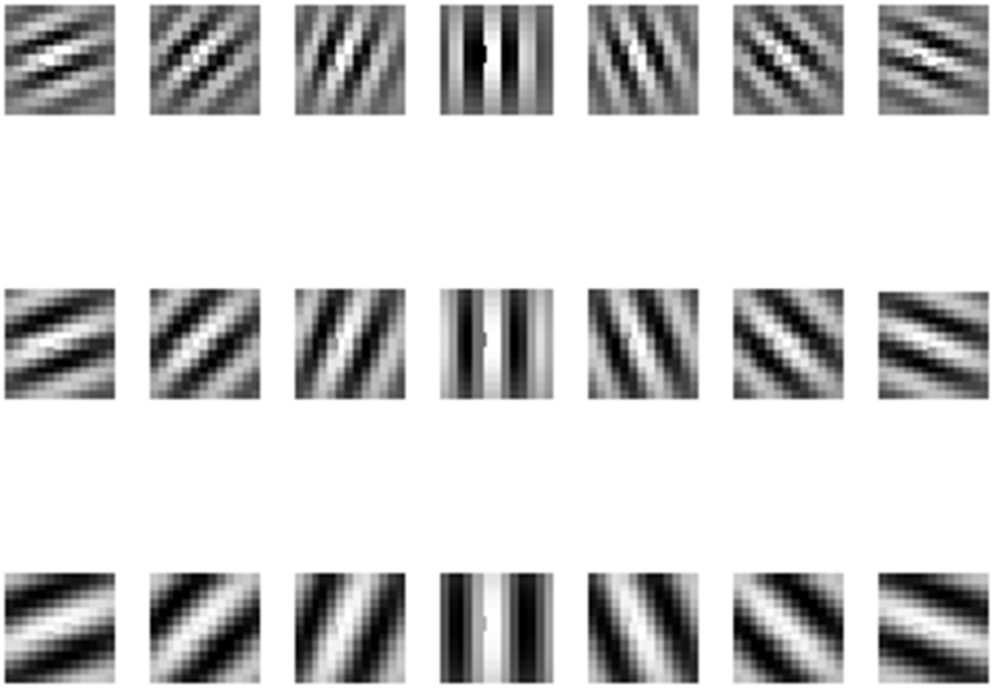

Fig. 5.3. The real part of Gabor filter family of 21 wavelets (feature images) obtained for a sample HEM IROI image with scales (0, 1, 2) from top to bottom and orientations (22.7°, 45°, 67.5°, 90°, 112.5°, 135°, 157.5°) from left to right.

5.4.3 Spatial Filtering Based Texture Features (F75- F86)

The Laws' texture features are spatial filtering based texture descriptors which are used to determine the texture properties of a ROI, by performing local averaging (L), edge detection (E), spot detection (S), wave detection (W), and ripple detection (R) in texture [2, 8, 63, 74]. Laws' texture features can be computed by using special 1-D filters of length 3, 5, 7, and 9 as shown in Table 5.4.

Table 5.4. Description of Laws' masks of different lengths.

Length of 1-D filter	1-D filter coefficients	No. of 2D Laws' masks	TRs obtained from identical filter pairs	Total TRs
3	L3=[1, 2, 1] E3=[-1, 0, 1] S3=[1-, 2, -1]	9	3	6
5	L5= [1, 4, 6, 4, 1] E5= [-1, -2, 0, 2, 1] S5= [-1, 0, 2, 0, -1] W5= [-1, 2, 0, -2 1] R5= [1, -4, 6, -4, 1]	25	10	15
7	L7= [1, 6, 15, 20, 15, 6, 1] E7= [-1 -4, -5, 0, 5, 4, 1] S7= [-1, -2, 1, 4, 1, -2, -1]	9	3	6
9	L9= [1, 8, 28, 56, 70, 56, 28, 8, 1] E9= [1, 4, 4, -4, -10, -4, 4, 4, 1] S9= [1, 0, -4, 0, 6, 0, -4, 0, 1] W9= [1, -4, 4, -4, -10, 4, 4, -4, 1] R9= [1, -8, 28, -56, 70, -56, 28, -8, 1]	25	10	15

Note: TRs: rotational invariant texture images.

Different filter lengths correspond to different resolutions for extraction of texture features from a ROI. In the present work, 1-D filters of length 3, i.e., L3 = [1, 2, 1], E3 = [-1, 0, 1], and S3 = [-1, 2, -1], have been considered for analysis. A total of nine 2-D filters are generated by combining these 1-D filters as shown in Figure 5.4.

L3L3	E3L3	S3L3
L3E3	E3E3	S3E3
L3S3	E3S3	S3S3

Fig. 5.4. Nine 2-D Laws' masks.

The classification of HEM and HCC lesions was initially attempted by Laws' masks of all the lengths i.e., 3, 5, 7, and 9. It was observed that the features derived by Laws' mask of length 3 resulted in better discrimination between HEM and HCC lesions. Therefore, in the present work, Laws' masks of length 3 have been considered.

For the detection and characterization of HEM and HCC initially, 3 TFVs are computed using FOS, GLCM, GLRLM, FPS, GWT and Laws' texture feature extraction methods. The description of these TFVs is given in Table 5.5.

Table 5.5 Description of TFVs.

TFVs	Description	*l*
TFV1	TFV consisting of 86 texture features (6 FOS, 13 GLCM, 11 GLRLM, 2 FPS, 42 Gabor, 12 Laws' features).	86
TFV2	TFV consisting of 86 texture ratio features (6 FOS, 13 GLCM, 11 GLRLM, 2 FPS, 42 Gabor, 12 Laws' features).	86
TFV3	Combined TFV consisting of 86 texture features (TFV1) and 86 texture ratio features (TFV2).	172

Note: TFVs: Texture Feature Vectors, *l*: Length of TFVs.

5.5. Results

For implementing the above CAD system design rigorous experiments were conducted. A brief description of these experiments is given in Table 5.6. The performance of the CAD system design has been compared with respect to overall classification accuracy (OCA), individual class accuracy (ICA), and the computational efficiency.

The flow chart for design of CAD system for classification of HEM and HCC lesions is shown in Fig. 5.5.

Table 5.6. Description of experiments carried out in the present work.

Experiment No.	Description
Experiment 1	To evaluate the performance of TFV1 with SVM and SSVM classifier.
Experiment 2	To evaluate the performance of TFV2 with SVM and SSVM classifier.
Experiment 3	To evaluate the performance of TFV3 with SVM and SSVM classifier.
Experiment 4	To evaluate the computational efficiency of SVM and SSVM classifier with TFV3.

Note: TFV: Texture feature vector.

5.5.1 Experiment 1: To evaluate the performance of TFV1 with SVM and SSVM classifier.

In this experiment, classification performance of TFV1 consisting of 86 IROI texture features has been evaluated using SVM and SSVM classifier. The results are reported in Table 5.7. It can be observed that the SVM classifier yields OCA of 52.9 % with ICA values of 90 % and 75 % for HEM and HCC classes, respectively. The SSVM classifier yields OCA of 72.9 % with ICA values of 46.6 % and 92.5 % for HEM and HCC classes, respectively.

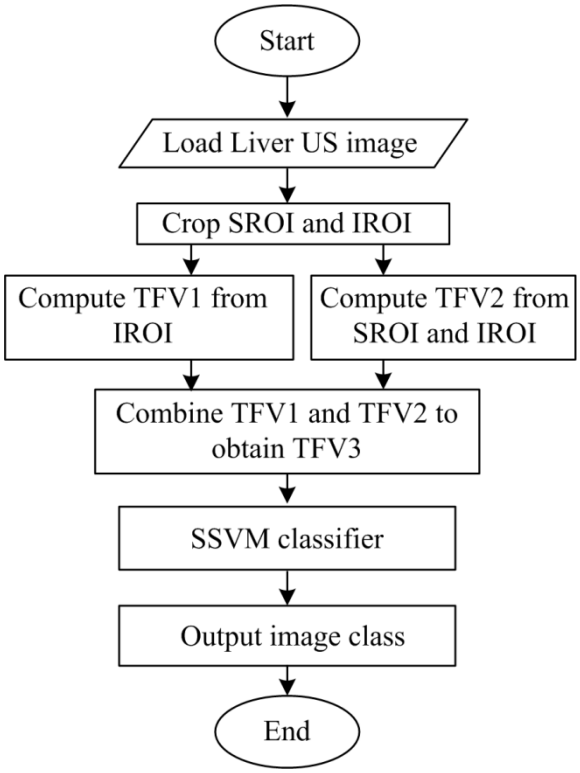

Fig. 5.5 Flow chart for design of CAD system for classification of HEM and HCC lesions.

Table 5.7. Classification performance of TFV1 with SVM and SSVM classifier.

TFV (*l*)	Classifier Used	CM			OCA (%)	ICA_{HEM} (%)	ICA_{HCC} (%)
			HEM	HCC			
TFV1 (86)	SVM	HEM	27	3	52.9	90.0	75.0
		HCC	30	10			
TFV1 (86)	SSVM	HEM	14	16	72.9	46.6	92.5
		HCC	3	37			

Note: TFV1: Texture feature vector 1 (consisting of 86 IROI texture features only); *l*: Length of TFV1; CM: Confusion Matrix; OCA: Overall classification accuracy; ICA: Individual Class Accuracy; ICA_{HEM}: ICA of HEM class; ICA_{HCC}: ICA of HCC class.

5.5.2 Experiment 2: To evaluate the performance of TFV2 with SVM and SSVM classifier

In this experiment, classification performance of TFV2 consisting of 86 texture ratio features has been evaluated using SVM and SSVM classifier. The results are reported in Table 5.8. It can be observed that the SVM classifier yields OCA of 77.1 % with ICA values of 50.0 % and 97.5 % for HEM and HCC classes, respectively. The SSVM classifier yields OCA of 91.4 % with ICA values of 90 % and 92.5 % for HEM and HCC classes, respectively.

5.5.3 Experiment 3: To evaluate the performance of TFV3 with SVM and SSVM classifier

In this experiment, the combined TFV i.e., TFV3 consisting of 172 features (86 IROI texture features + 86 texture ratio features) has been evaluated by using SVM and SSVM

classifier. The results are reported in Table 5.9. It can be observed that the SVM classifier yields OCA of 92.9 % with ICA values of 93.3 % and 92.5 % for HEM and HCC classes, respectively. The SSVM classifier yields OCA of 94.3 % with ICA values of 96.6 % and 92.5 % for HEM and HCC classes, respectively.

Table 5.8. Classification performance of TFV2 with SVM and SSVM classifier.

TFV (*l*)	Classifier Used	CM			OCA (%)	ICA_{HEM} (%)	ICA_{HCC} (%)
			HEM	HCC			
TFV2 (86)	SVM	HEM	15	15	77.1	50.0	97.5
		HCC	1	39			
TFV2 (86)	SSVM	HEM	27	3	91.4	90.0	92.5
		HCC	3	37			

Note: TFV2: Texture feature vector 2 (consisting of 86 texture ratio features only); *l*: Length of TFV2; CM: Confusion Matrix; OCA: Overall classification accuracy; ICA: Individual Class Accuracy; ICA_{HEM}: ICA of HEM class; ICA_{HCC}: ICA of HCC class.

Table 5.9. Classification performance with of TFV3 with SVM and SSVM classifier.

TFV (*l*)	Classifier Used	CM			OCA (%)	ICA_{HEM} (%)	ICA_{HCC} (%)
			HEM	HCC			
TFV3 (86)	SVM	HEM	28	2	92.9	93.3	92.5
		HCC	3	37			
TFV3 (86)	SSVM	HEM	29	1	94.3	96.6	92.5
		HCC	3	37			

Note: TFV3: Texture feature vector 3 (consisting of 172 texture features, i.e., TFV1 and TFV2); *l*: Length of TFV3; CM: Confusion Matrix; OCA: Overall classification accuracy; ICA: Individual Class Accuracy; ICA_{HEM}: ICA of HEM class; ICA_{HCC}: ICA of HCC class.
It can be observed that the results obtained by SSVM classifier (shaded in gray) are better in comparison with SVM classifier.

5.5.4 Experiment 4: To evaluate the computational efficiency of SVM and SSVM classifier with TFV3.

From the results of the exhaustive experiments carried out in the study, it can be observed that TFV3 i.e., combined TFV yields highest OCA value in comparison with the OCA value yielded by TFV1 and TFV2. Therefore, the computational efficiency of SVM and SSVM classifier with only TFV3 has been evaluated. Further, since the time taken for computing TFV3 is same for both the CAD system designs i.e., SVM based CAD system and SSVM based CAD system, the time taken for prediction of 70 cases of testing dataset of TFV3 is considered for evaluating the computational efficiency. It was observed that the proposed SSVM based CAD system design is computationally more efficient than SVM based CAD system design as the time taken for prediction was 5.1 µs for SVM classifier and 3.4 µs for SSVM classifier using MATLAB (version 7.6.0.324 R2008a) with PC configuration Intel® Core™ I3-M 370, 2.40GHz with 3 GB RAM.

5.6 Discussion

Misclassification Analysis: Analysis of five misclassified cases out of 70 cases (i.e., 5/70) for SVM based CAD system design and four misclassified cases out of 70 cases (i.e., 4/70) for SSVM based CAD system design is given in Table 5.10. It can be observed that same ICA values of 100 %, 100 % and 90.3 %, are obtained for typical HEM, SHCC and LHCC cases with both SVM and SSVM based CAD system designs. However, it is worth mentioning that for atypical HEM class the SSVM based CAD system design yields higher ICA value of 96 % in comparison to 92 % as yielded by SVM based CAD system design. It can also be seen from Table 5.9 that the proposed SSVM based CAD system design yields higher OCA of 94.3 % in comparison to 92.9 % as yielded by SVM based CAD system design.

Since, US offers limited sensitivity for detection of SHCCs and also given the fact that differential diagnosis between atypical HEM and HCC cases is considerably difficult; therefore, the improvement in ICA values for atypical HEMs and HCC cases is highly desirable. Further, it can be observed that all the SHCC cases have been correctly classified by both the CAD system designs (i.e., the ICA value for SHCC is 100 %).

Table 5.10. Misclassification analysis of 70 cases of testing dataset with SVM and SSVM classifier.

Misclassification analysis of HEM cases		
	SVM	SSVM
Total HEM cases	30	30
Typical HEM cases	5	5
Atypical HEM cases	25	25
Correctly classified cases	28	29
Misclassified cases	2	1
ICA_{HEM}	93.3 %	96.6 %
HEM misclassified cases	2 out of 25 atypical HEM cases	1 out of 25atypical HEM cases
$ICA_{TypicalHEM}$	100 %	100 %
$ICA_{AtypicalHEM}$	92 %	96 %
Misclassification analysis of HCC cases		
	SVM	SSVM
Total HCC cases	40	40
Small HCC cases	9	9
Large HCC cases	31	31
Correctly classified cases	37	37
Misclassified cases	3	3
ICA_{HCC}	92.5 %	92.5 %
HCC misclassified cases	3 out of 31 LHCC cases	3 out of 31 LHCC cases
ICA_{SHCC}	100 %	100 %
ICA_{LHCC}	90.3 %	90.3 %

Note: ICA: Individual Class Accuracy; ICA_{HEM}: ICA of HEM class; $ICA_{TypicalHEM}$: ICA of Typical HEM class; $ICA_{AtypicalHEM}$: ICA of Atypical HEM class; ICA_{HCC}: ICA of HCC class; ICA_{SHCC}: ICA of Small HCC class; ICA_{LHCC}: ICA of Large HCC class.
It can be observed that the ICA value of atypical HEM class (shaded in gray) has improved with SSVM classifier.

Overall it can be observed that the SSVM based CAD system outperforms the SVM based CAD system with respect to the (*a*) OCA value, (*b*) ICA value for the atypical HEM cases, and (*c*) computational efficiency.

The participating radiologists were of the view that the results yielded by proposed SSVM based CAD system design are quite convincing keeping in view that the comprehensive and diversified database (consisting of typical and atypical HEMs as well SHCC and LHCCs cases) used in present work.

5.7 Concluding Remarks

In the present work, rigorous experiments were carried out for the design of an efficient CAD system for characterization of HEM and HCC lesions using B-Mode US images. The following main conclusions can be drawn:

(*a*) The texture of the region surrounding the lesion contributes significantly towards the differential diagnosis of HEM and HCC lesions.

(*b*) The proposed SSVM based CAD system design is better in comparison to the SVM based CAD system design in terms of the OCA value, ICA values for atypical HEM class and computational efficiency.

The promising results yielded by proposed SSVM based CAD system design indicate its usefulness to assist radiologists for the differential diagnosis of HEM and HCC lesions during routine clinical practice.

Chapter 6

Hierarchical CAD System Design for Classification of benign and malignant FLLs

6.1. Introduction

The aim of the present study is to develop a hierarchical CAD (HCAD) system for the differential diagnosis between primary benign (i.e., HEM), primary malignant (i.e., HCC), and secondary malignant (i.e., MET) lesions. In the present work, benign FLL i.e., HEM is considered, as among other primary benign liver lesions, HEM is the most commonly occurring primary benign lesion [1- 3]. Among malignant FLLs, the present study is focused on characterization of HCC (i.e., most commonly occurring primary malignant FLL [16- 18]) and MET (i.e., most commonly occurring secondary malignant FLL [1- 3, 8, 9, 12]).

There are certain limitations concerning the use of B-mode US for characterization of FLLs, (*a*) limited sensitivity for detection of small FLLs (< 2 cm) developed on top of cirrhotic liver [1, 2, 7, 8, 10- 15], (*b*) overlapping sonographic appearances of atypical HEM, HCC and atypical MET lesions, (*c*) limited sensitivity for detection of isoechoic lesions with the slim difference in contrast between regions inside and outside the lesion [1, 12]. It is expected that the extraction of discriminatory features which are difficult to extract visually, followed by an efficient classifier design with a comprehensive data set consisting of representative images for various sub classes can reduce these limitations.

In the present work, an investigation of contribution made by texture information present in the regions inside and outside of the lesion has been carried out for characterization of primary benign and malignant FLLs. For the classification task, SSVM classifier has been used [66, 67].

6.2. Data Set Description

In order to carry out the present work, 76 B-mode liver US images consisting of (*a*) 16 HEM images with 16 solitary HEM lesions consisting of 10 typical and 6 atypical HEM lesions, (*b*) 28 HCC images with 28 solitary HCC lesions consisting of 13 SHCC and 15 LHCC lesions, and (*c*) 32 MET images with 32 solitary MET lesions consisting of 12 typical and 20 atypical MET lesions, have been used. The image dataset description is

given in Table 6.1. The final dataset consisting of total 255 IROIs and 76 SROIs was stored in Intel® Core™ I3-M 370, 2.40 GHz with 3 GB RAM.

Table 6.1. Data Set Description.

Clinically acquired B-mode liver US images (76) **Total IROIs: 255, Total SROIs: 76**			
	HEM	**HCC**	**MET**
Total Images	16 Typical HEM: 10 Atypical HEM: 6	28 SHCC: 13 LHCC: 15	32 Typical MET: 12 Atypical MET: 20
Total Lesions	16	28	32
Total IROIs	70 Typical HEM IROIs: 27 Atypical HEM IROIs: 43	90 SHCC IROIs: 19 LHCC IROIs: 71	95 Typical MET IROIs: 14 Atypical MET IROIs: 81
Total SROIs	16	28	32

Note: SHCC: Small Hepatocellular Carcinoma (size varies from 1.5 to 1.9 cm); LHCC: Large Hepatocellular Carcinoma (size varies from 2.1 to 5.6 cm).

To design the efficient HCAD system, it is ensured that the training data should include lesions from image sub-classes i.e., typical and atypical HEM and MET lesions, and SHCCs as well as LHCCs lesions. Each image class was further divided into two sets i.e., (*a*) training dataset, and (*b*) testing dataset. In order to avoid biasing, training ROIs were taken from first set while testing ROIs were taken from other set. The brief description of training and testing dataset is given in Table 6.2.

Table 6.2. Training and Testing Dataset Description for HEM, HCC and MET classes.

Training Data Set Description			
	HEM	**HCC**	**MET**
Total images (44)	10	16	18
Total lesions	10 Typical HEM lesions: 7 Atypical HEM lesions: 3	16 SHCC lesions: 7 LHCC lesions: 9	18 Typical MET lesions: 7 Atypical MET lesions: 11
Total IROIs (140)	40 Typical HEM IROIs: 22 Atypical HEM IROIs: 18	50 SHCC IROIs: 10 LHCC IROIs: 40	50 Typical MET IROIs: 9 Atypical MET IROIs: 41
Total SROIs (44)	10	16	18
Testing Data Set Description			
Total images (32)	6	12	14
Total lesions	6 Typical HEM lesions: 3 Atypical HEM lesions: 3	12 SHCC lesions: 7 LHCC lesions: 9	14 Typical MET lesions: 5 Atypical MET lesions: 9
Total IROIs (135)	40 Typical HEM IROIs: 22 Atypical HEM IROIs: 18	50 SHCC IROIs: 10 LHCC IROIs: 40	45 Typical MET IROIs: 5 Atypical MET IROIs: 40
Total SROIs (40)	10	16	14

6.3. Proposed CAD System Design

The CAD system for the characterization of HEM, HCC and MET have been proposed in the present study. In order to implement the present HCAD system design, the database of 255 non-overlapping IROIs and 76 SROIs was extracted from 76 B-mode liver US liver images. The CAD system includes feature extraction methods and classification module for the differential diagnosis of HEM, HCC and MET lesions.

In feature extraction module, texture features are computed from 255 IROIs and 76 SROIs using (*a*) FOS and higher order statistics i.e., GLRLM features, (*b*) spectral features such as FPS and GWT features, and (*c*) spatial filtering based Laws' texture features. The texture feature set of 146 texture features (consisting of 73 texture IROI features and 73 texture ratio features) is considered for analysis. The texture feature set is further divided into training and testing data feature set. The bifurcation of ROIs of each class in training and testing data feature set is given in Table 6.2. In classification module, SSVM classifier has been used for the classification task.

6.3.1 Feature Extraction Module

Two types of features are considered for analysis i.e. texture features computed from IROIs and texture ratio features computed by taking the ratio of texture feature computed from IROI and texture feature computed from corresponding SROI. In the present work initially, a wide variety of texture features are extracted by using statistical, spectral and spatial filtering based feature extraction methods as shown in Fig. 6.1.

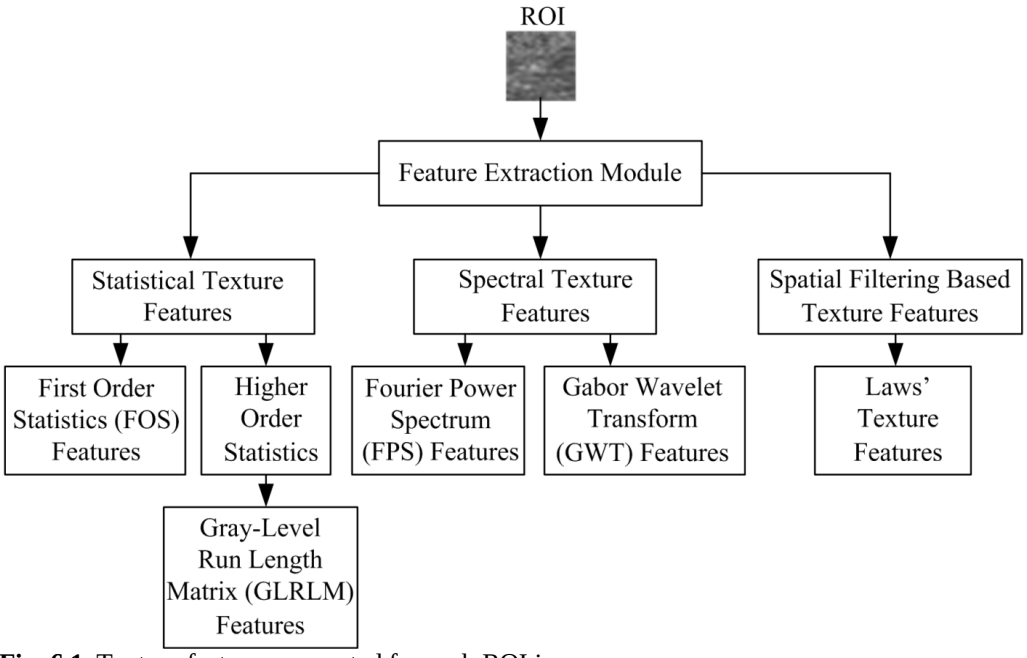

Fig. 6.1. Texture features computed for each ROI image.

6.3.2 Classification Module

In the present work, the classification task has been carried out in two ways (a) Three class classification task carried out by using a single SSVM based three class classifier, and (b) Three class classification task carried out by using two SSVM based binary classifiers arranged in a hierarchical framework. These two SSVM classifiers provide stepwise classification for the generalized three class classification problem in two stages. In the first stage, SSVM binary classifier 1 was used to classify test cases from all the three classes into primary benign (i.e., HEM) or malignant cases (i.e., HCC or MET). The predicted malignant cases were then provided as the input to SSVM binary classifier 2. The second classifier further classifies the malignant cases into primary malignant i.e., HCC class or secondary malignant i.e., MET cases. The architecture of classification module is shown in Fig. 6.2.

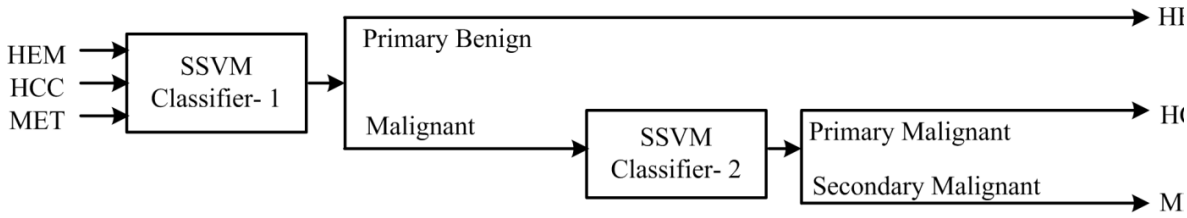

Fig. 6.2. Architecture of **c**lassification module.

6.4 Results

Two stage classification tasks were carried out corresponding to two SSVM based classifiers arranged in a hierarchical framework. Each binary classifier was trained independently. The dataset description and the bifurcation of dataset into disjoint training and testing datasets for each binary classifier is shown in Table 6.2. For implementing the above CAD system design various experiments were conducted as given in Table 6.3.

Table 6.3. Description of experiments carried out in the present work.

Experiment No.	Description
1.	To evaluate the performance of three class SSVM classifier design for characterization of benign and malignant FLLs.
2.	To evaluate the performance of SSVM based hierarchical classifier design for characterization of benign and malignant FLLs.
3.	Performance comparison of SSVM based three class classifier design and SSVM based hierarchical classifier design for characterization of benign and malignant FLLs.

The experimental flow chart for design of HCAD system for classification of primary benign, primary malignant and secondary malignant FLLs is shown in Fig. 6.3.

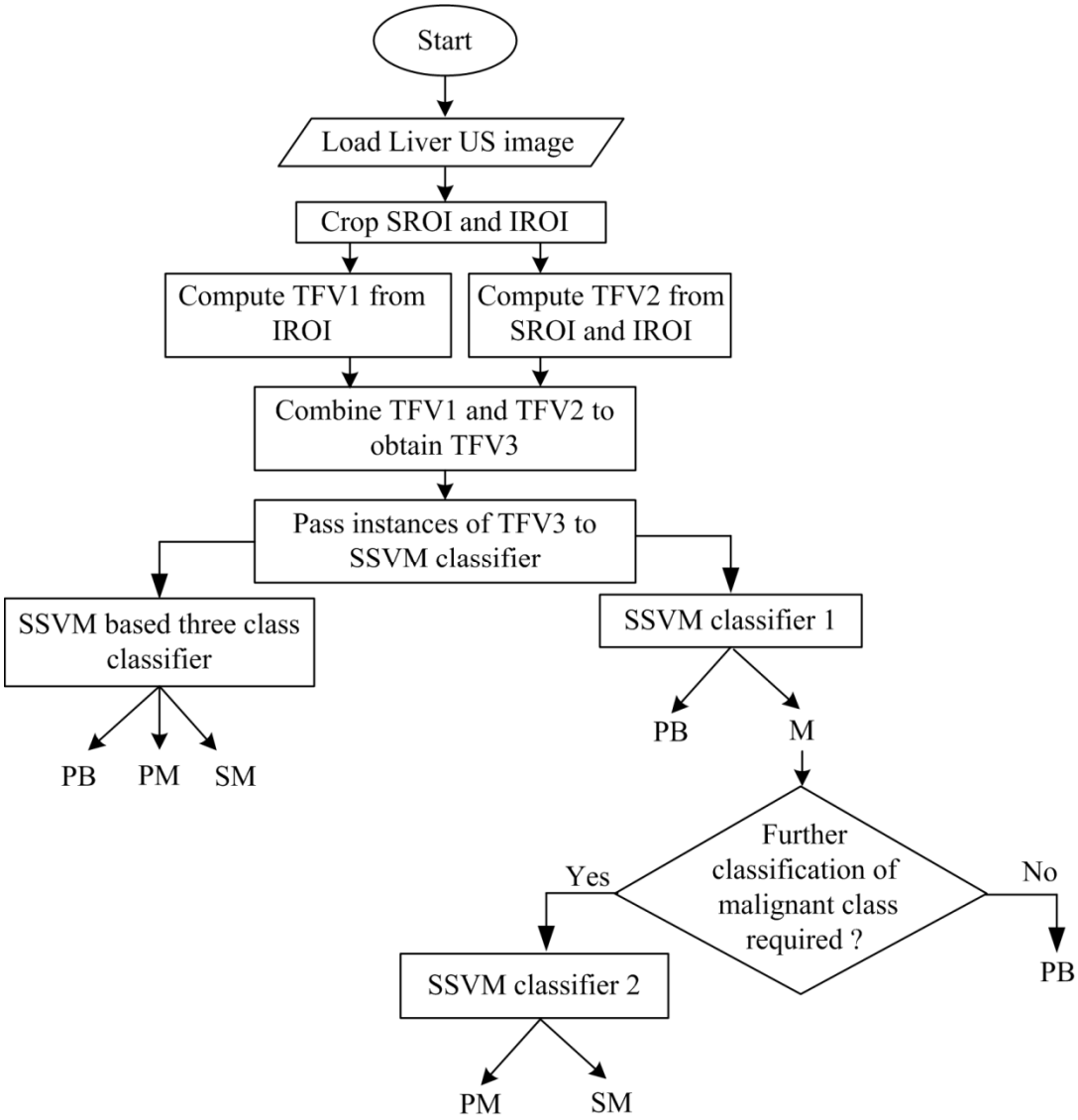

Fig. 6.3. Experimental work flow for design of HCAD system for classification of benign and malignant lesions.

6.4.1 Experiment 1: To evaluate the performance of three class SSVM classifier design for characterization of benign and malignant FLLs.

In this experiment, classification performance of TFVs (consisting of TFV1, TFV2, and TFV3) has been evaluated using SSVM classifier for three class classification of primary benign, primary malignant and secondary malignant FLLs. The results are reported in Table 6.4. It can be observed that OCA values of 63.5 %, 75.7 % and 82.6 % has been achieved with TFV1, TFV2 and TFV3 respectively. The ICA values obtained with respect to TFV3 are 83.3 %, 72.5 %, and 91.1 % for primary benign, primary malignant and secondary malignant cases.

Table 6.4. Three class classification performance of TFVs with SSVM classifier.

TFV (*l*)	CM				OCA (%)	ICA_{PB} (%)	ICA_{PM} (%)	ICA_{SM} (%)
		PB	PM	SM				
TFV1 (73)	PB	26	3	1	63.5	86.7	42.5	66.7
	PM	11	17	12				
	SM	5	10	30				
TFV2 (73)	PB	29	1	0	75.7	96.7	82.5	55.6
	PM	2	33	5				
	SM	1	19	25				
TFV3 (146)	PB	25	0	5	82.6	83.3	72.5	91.1
	PM	1	29	10				
	SM	4	0	41				

Note: TFV: Texture feature vector; l: Length of TFV; TFV1: TFV 1 containing IROI features only; TFV2: TFV 2 containing ratio features only; TFV3: combined TFV containing IROI features and ratio features; CM: Confusion Matrix; OCA: Overall classification accuracy; ICA: Individual Class Accuracy; ICAPB: ICA of Primary Benign class; ICAPM: ICA of Primary Malignant class; ICASM: ICA of Secondary Malignant class.

6.4.2 Experiment 2: To evaluate the performance of SSVM based hierarchical classifier design for characterization of benign and malignant FLLs.

In this experiment, classification performance of TFVs has been evaluated using SSVM based hierarchical classifier for binary classification of primary benign and malignant FLLs. The CAD system is consisted of two SSVM based CAD system arranged in hierarchical framework. The results of SSVM classifier 1 and SSVM classifier 2 are reported in Table 6.5 and Table 6.6 respectively. The OCA values yielded by SSVM classifier at node 1 for TFV1, TFV2, and TFV3 are 85.2 %, 96.5 %, and 97.4 % respectively. The ICA values obtained with respect to TFV3 are 90 %, and 100 % for primary benign and malignant cases. The OCA values yielded by SSVM classifier at node 2 for TFV1, TFV2, and TFV3 are 69.4 %, 80 %, and 89.4 % respectively. The ICA values obtained with respect to TFV3 are 77.5 %, and 100 % for primary malignant and secondary malignant cases.

Table 6.5. Classification performance of TFVs with SSVM classifier 1.

TFV (*l*)	CM			OCA (%)	ICA_{PB} (%)	ICA_{M} (%)
		PB	M			
TFV1 (73)	PB	14	16	85.2	46.7	98.9
	M	1	84			
TFV2 (73)	PB	26	4	96.5	86.7	100
	M	0	85			
TFV3 (146)	PB	27	3	97.4	90.0	100
	M	0	85			

Note: TFV: Texture feature vector; *l*: Length of TFV; TFV1: TFV 1 containing IROI features only; TFV2: TFV 2 containing ratio features only; TFV3: combined TFV containing IROI features and ratio features; CM: Confusion Matrix; ICA_{PB}: ICA of Primary Benign class; ICA_{M}: ICA of Malignant class.

Table 6.6. Classification performance of TFVs with SSVM classifier 2.

TFV (*l*)		CM		OCA (%)	ICA_{PM} (%)	ICA_{SM} (%)
		PM	SM			
TFV1 (73)	PM	34	6	69.4	85.0	55.6
	SM	20	25			
TFV2 (73)	PM	36	4	80.0	90.0	71.1
	SM	13	32			
TFV3 (146)	PM	31	9	89.4	77.5	100
	SM	0	45			

Note: TFV: Texture feature vector; *l*: Length of TFV; TFV1: TFV 1 containing IROI features only; TFV2: TFV 2 containing ratio features only; TFV3: combined TFV containing IROI features and ratio features; CM: Confusion Matrix; OCA: Overall classification accuracy; ICA: Individual Class Accuracy; ICA_{PM}: ICA of Primary Malignant class; ICA_{SM}: ICA of Secondary Malignant class.

6.4.3 Experiment 3: Performance comparison of SSVM based three class classifier design and SSVM based hierarchical classifier design for characterization of benign and malignant FLLs.

In this experiment, performance comparison of SSVM based three class classifier design and SSVM based hierarchical classifier design for characterization of benign and malignant FLLs has been carried out. The results are reported in Table 6.7. The OCA value achieved with three class classifier and hierarchical classifier are 82.6 % and 89.6 %, respectively. The OCA for hierarchical classifier is obtained by adding the total misclassification obtained at each node of SSVM classifiers. The misclassifications obtained for SSVM based three class classifier design is 20/115 (i.e., 20 cases misclassified out of 115 test instances) and for SSVM based hierarchical classifier design is 12/115 (i.e., 12 cases misclassified out of 115 test instances). The misclassifications yielded by SSVM classifier 1 and SSVM classifier 2 is 3/115 (i.e., 3 cases misclassified out of 115 test instances) and 9/85 (i.e., 9 cases misclassified out of 85 test instances), respectively.

Table 6.7. Classification performance of TFV3 with SSVM based multiclass classifier and SSVM based hierarchical classifier.

Classifier used	CM				OCA (%)	Misclassification
		PB	PM	SM		
SSVM multiclass classifier	PB	25	0	5	82.6	20/115
	PM	1	29	10		
	SM	4	0	41		
Classifier used	**CM**			**CA (%)**	**OCA (%)**	**Misclassification**
SSVM hierarchical classifier 1		PB	M		89.6	12/115
	PB	27	3	97.4 (3/115)		
	M	0	85			
SSVM hierarchical classifier 2		PM	SM			
	PM	31	9	89.4 (9/85)		
	SM	0	45			

The misclassification analysis for SSVM based three class classifier design and SSVM based hierarchical classifier design for characterization of benign and malignant FLLs is reported in Table 6.8. The SSVM based three class classifier yielded total 20 misclassifications i.e., 5, 11, and 4 for primary benign, primary malignant and secondary malignant classes, respectively. A total of 12 (12 out of 115 cases) misclassifications have been yielded by SSVM based hierarchical classifier including 3 (3 out of 30 cases) and 9 (9 out of 40 cases) misclassification cases for primary benign and primary malignant classes, respectively. It is worth mentioning that all the cases of secondary malignant class have classified correctly.

Table 6.8. Misclassification analysis of 115 cases of testing dataset with SSVM based hierarchical classifier.

Misclassification analysis of HEM cases			
	PB	PM	SM
Total cases	30	40	45
	Typical HEM: 5	Small HCC: 9	Typical MET: 5
	Atypical HEM: 25	Large HCC: 31	Atypical MET: 45
ICA	ICA_{PB} = 90 %	ICA_{PM} = 77.5 %	ICA_{SM} = 100 %
	$ICA_{TypicalHEM}$ = 100 %	ICA_{SHCC} = 77.8 %	$ICA_{TypicalMET}$ = 100 %
	$ICA_{AtypicalHEM}$ = 88 %	ICA_{LHCC} = 77.4 %	$ICA_{AtypicalMET}$ = 100 %
Correctly classified cases	27	31	45
Misclassified cases	3	9	0
Misclassified cases description	3 out of 25 atypical HEM cases	2 out of 9 SHCC cases 7 out of 31 LHCC cases	-

Note: ICA: Individual Class Accuracy; ICA_{PB}: ICA of primary benign class; $ICA_{TypicalHEM}$: ICA of Typical HEM class; $ICA_{AtypicalHEM}$: ICA of Atypical HEM class; ICA_{PM}: ICA of primary malignant class; ICA_{SHCC}: ICA of Small HCC class; ICA_{LHCC}: ICA of Large HCC class; ICA_{SM}: ICA of secondary malignant class; $ICA_{TypicalMET}$: ICA of Typical MET class; $ICA_{AtypicalMET}$: ICA of Atypical MET class.

6.5 Concluding Remarks

In the present study, an efficient SSVM based hierarchical CAD system for the classification of benign and malignant FLLs of gray scale B-mode liver US images has been proposed. By visualizing the performance of SSVM based hierarchical classifier design, some interesting facts are observed:

(*a*) The decision is made at SSVM classifier 1, whether the ROI selected by radiologists is benign or malignant. If further investigation of malignant instances as HCC or MET is required then the instance will be passed to second SSVM based classifier.

(*b*) Three class classifier design creates three binary classifiers between PB/PM, PM/SM, and SM/PB, while two binary classifiers were created internally at each node for SSVM based hierarchical classifier design i.e., PB/M and PM/SM binary classifiers.

Chapter 7

Conclusion and Future Scope

The main objective of the research work presented in the thesis is to enhance the diagnostic potential of conventional gray scale B-Mode ultrasound for diagnosis of liver diseases by removing speckle noise from the US images and by developing efficient CAD system designs using a comprehensive and representative image database. The present work has been carried out for despeckling of performance evaluation of B-Mode liver US images. The CAD system for the differential diagnosis between primary benign and primary malignant has been evaluated. Also, a hierarchical CAD system design has been proposed in the present work for characterization of benign and malignant liver lesions.

7.1. Conclusion- Despeckle filtering and performance evaluation of B-Mode liver US images

Although Speckle noise in ultrasound images makes the subjective diagnosis difficult but it is a well known fact that speckle in US images also contains diagnostic information so the despeckling of US images should be carried out such that the diagnostic features such as edges and structure of the image is preserved while the speckle is removed from the uniform areas. Subjective analysis for performance evaluation of Despeckle filtering algorithms is difficult as it requires the time of experienced medical experts and is also subjected to inter and intra observer variability. Objective analysis for performance evaluation offers a more accurate method for performance evaluation of Despeckle filtering algorithms. From the exhaustive experiments carried out in the present work it can be observed that the liver US images despeckled by Lee-sigma method yield the highest values for PSNR, FOM, and SSIM metrics. Thus, it can be concluded that US liver images processed by Lee-Sigma despeckling algorithm results in better edge and structure preservation while providing adequate smoothing in the uniform areas.

7.2. Conclusion- Design of an Efficient CAD System for Characterization of primary benign and primary malignant liver lesions

Rigorous experiments were carried out for the design of an efficient CAD system for characterization of HEM and HCC lesions using B-Mode US images. The following main conclusions can be drawn:

(*a*) The texture of the region surrounding the lesion contributes significantly towards the differential diagnosis of HEM and HCC lesions.

(*b*) The proposed SSVM based CAD system design is better in comparison to the SVM based CAD system design in terms of the OCA value, ICA values for atypical HEM class and computational efficiency.

The promising results yielded by proposed SSVM based CAD system design indicate its usefulness to assist radiologists for the differential diagnosis of HEM and HCC lesions during routine clinical practice.

7.3. Conclusion- Design of an Efficient Hierarchical CAD System for Characterization of benign and malignant liver lesions

An efficient SSVM based hierarchical CAD system for the classification of benign and malignant FLLs of gray scale B-mode liver US images has been proposed. By visualizing the performance of SSVM based hierarchical classifier design, some interesting facts are observed:

(*a*) The decision is made at SSVM classifier 1, whether the ROI selected by radiologists is benign or malignant. If further investigation of malignant instances as HCC or MET is required then the instance will be passed to second SSVM based classifier.

(*b*) Three class classifier design creates three binary classifiers between PB/PM, PM/SM, and SM/PB, while two binary classifiers were created internally at each node for SSVM based hierarchical classifier design i.e., PB/M and PM/SM binary classifiers.

7.4. Limitations and Future Scope

The limitation is that there is no benchmark data available and the present work has been carried out on real time liver US images. Therefore, it cannot be compared directly with any standard results.

Following are the recommendations for future work:

(*i*) The present work has been carried out on B-Mode liver US images processed by Lee-Sigma despeckling algorithm which results in better edge and structure preservation while providing adequate smoothing in the uniform areas. However the improvement with respect to classification of primary and secondary malignant FLLs by preprocessing the images with Lee-sigma method remains to be investigated.

(*iii*) In the present work, ROIs from liver US images are extracted manually. An algorithm for automatic ROI extraction can be developed by employing various pattern recognition concepts to identify the lesion and then extract an ROI of some specified size within its boundary.

(*iv*) The performance of the proposed algorithms remains to be tested on images of different resolutions as the images used in the present work has been acquired from the single US machine.

Publications from the Present Work

Referred Journal Publications

1) Nimisha Manth and Jitendra Virmani, "Evaluation of Despeckle Filtering Algorithms for B-Mode Liver Ultrasound Images", *International Journal of Signal and Imaging Systems Engineering*. (Publisher: Inderscience) [Communicated].
2) Nimisha Manth and Jitendra Virmani, "A SSVM based CAD system for primary benign and primary malignant focal liver lesions using B-Mode Liver Ultrasound Images", *Journal of Digital Imaging*. (Publisher: Springer) [Communicated].
3) Nimisha Manth and Jitendra Virmani, "Computer Aided Classification system for benign and malignant focal hepatic lesions", *National Academy Science Letters*. (Publisher: Springer) [Communicated].

Referred Conference Publications

1) Nimisha Manth and Jitendra Virmani, "Despeckle filtering: Performance evaluation for malignant focal hepatic lesions", in *Computing for Sustainable Global Development (INDIACom), 2015 2nd International Conference*. [Accepted for Publication].

[1] J. Harding, and M. Callaway, "Ultrasound of focal liver lesions", *RAD Magazine*, Vol. 36, No. 424, pp. 33– 34, 2010.

[2] J. Virmani, V. Kumar, N. Kalra, and N. Khandelwal, "A comparative study of computer-aided classification systems for focal hepatic lesions from B-mode ultrasound", *Journal of Medical Engineering and Technology*, Vol. 37, No. 4, pp. 229– 306, 2013.

[3] J. H. Pen, P. A. Pelckmans, Y. M. Van Maercke, H. R. Degryse, and A. M. De Schepper, "Clinical significance of focal echogenic liver lesions", *Gastrointest Radiol*, Vol. 1, No.1, pp. 61-66, 1986.

[4] S. Namasivayam, K. Salman, P. K. Mittal, D. Martin, and W. C. Small, "Hypervascular hepatic focal lesions: spectrum of imaging features", *Curr Probl Diagn Radiol*, Vol. 36, No. 3, pp. 107–123, 2007.

[5] V. Vilgrain, L. Boulos, M. P. Vullierme, A. Denys, B. Terris, and Y. Menu, "Imaging of atypical hemangiomas of the liver with pathologic correlation", *Radiographics*, Vol. 20, No. 2, pp. 379–397, 2000.

[6] M. Tsurusaki, R. Kawasaki, M. Yamaguchi, K. Sugimoto, T. Fukumoto, Y. Ku, and K. Sugimura, " Atypical hemangioma mimicking hepatocellular carcinoma with a special note on radiological and pathological findings", *Jpn J Radiol*, Vol. 27, No. 3, pp. 156–160, 2009.

[7] J. Virmani, V. Kumar, N. Kalra, and N. Khandelwal, "Characterization of primary and secondary malignant liver lesions from B-mode ultrasound", *J Digit Imaging*, Vol. 26, No. 6, pp. 1058–1070, 2013.

[8] J. Virmani, V. Kumar, N. Kalra, and N. Khandelwal, "PCA-SVM based CAD system for focal liver lesions from B-mode ultrasound", *Def Sci J*, Vol. 63, No. 5, pp. 478–486, 2013.

[9] H. Yoshida, D. D. Casalino, B. Keserci, A. Coskun, O. Ozturk, and A. Savranlar, " Wavelet packet based texture analysis for differentiation between benign and malignant liver tumors in ultrasound images", *Phys Med Biol*, Vol. 48, No. 1, pp. 3735–3753, 2003.

[10] J. Bates – *Abdominal Ultrasound How Why and When*; Second Edition; Churchill Livingstone, Oxford, pp. 80- 107, 2004.

[11] R. B. Jeffery , and P.W. Ralls – *Sonography of Abdomen*; Raven, New York, 1995.

[12] D. A. Tiferes, and G. D'lppolito, "Liver neoplasms: imaging characterization", *Radiol Bras*, Vol. 41, No. 2, pp. 119–127, 2008.

[13] J. A. Soye, C. P. Mullan, S. Porter, H. Beattie, A. H. Barltrop, and W. M. Nelson, "The use of contrast-enhanced ultrasound in the characterization of focal liver lesions", *Ulster Med J*, Vol. 76, No. 1, pp. 22–25, 2007.

[14] M. Colombo, and G. Ronchi, "Focal Liver Lesions – Detection, Characterization, Ablation", Springer, Berlin, pp. 167–177, 2005.

[15] M. Di Martino, G. De Filippis, A. De Santis, D. Geiger, M. Del Monte, C. V. Lombardo, M. Rossi, S. G. Corradini, G. Mennini, and C. Catalano, "Hepatocellular carcinoma in cirrhotic patients: prospective comparison of US, CT and MR imaging", *Eur Radiol*, Vol. 23, No. 4, pp. 887–896, 2013.

[16] D. Mitrea, S. Nedevschi, M. Lupsor, M. Socaciu, and R. Badea, "Advanced classification methods for improving the automatic diagnosis of the hepatocellular carcinoma, based on ultrasound images", *Automation Quality and Testing Robotics (AQTR), 2010 IEEE Int Conf*, Vol. 2, No. 1, pp. 1-6, 2010.

[17] D. Mitrea, S. Nedevschi, M. Lupsor, M. Socaciu, and R. Badea, "Exploring texture-based parameters for noninvasive detection of diffuse liver diseases and liver cancer from ultrasound images", *In: Proceedings of MMACTEE'06 Proceedings of the 8th WSEAS Int Conf on Mathematical methods and computational techniques in electrical engineering*, pp. 259-265, 2006.

[18] D. Mitrea, S. Nedevschi, M. Lupsor, M. Socaciu, and R. Badea, "Improving the textural model of the hepatocellular carcinoma using dimensionality reduction methods", *Image and Signal Processing, 2009. CISP '09. 2nd International Congress on*, Vol. 1, No. 5, pp. 17-19, 2009.

[19] J. Virmani, V. Kumar, N. Kalra, and N. Khandelwal, "SVM-based characterization of liver ultrasound images using wavelet packet texture descriptors", *J Digit Imaging*, Vol. 26, No. 3, pp. 530–543, 2013.

[20] W. Scheible, B. B. Gossink, G. Leopold, "Gray scale echo graphic patterns of hepatic metastatic disease", *Am J Roentgenol*, Vol. 129, No. 1, pp. 983– 987, 1977.

[21] M. Tsurusaki, R. Kawasaki, M. Yamaguchi, K. Sugimoto, T. Fukumoto, Y. Ku, and K. Sugimura, "Atypical hemangioma mimicking hepatocellular carcinoma with a special

note on radiological and pathological findings", *Jpn J Radiol*, Vol. 27, No. 3, pp. 156–160, 2009.

[22] T. Albrecht, J. Hohmann, A. Oldenburg, and K. Wolf, "Detection and characterization of liver metastases", *Eur Radiol Suppl*, Vol.14, No. S8, pp. 25– 33, 2004.

[23] J. Virmani, V. Kumar, N. Kalra, and N. Khandelwal, "A rapid approach for prediction of liver cirrhosis based on first order statistics", *In: Proceedings of IEEE International Conference on Multimedia, Signal Processing and Communication Technologies, IMPACT-2011*, pp. 212-215, 2011.

[24] J. Virmani, V. Kumar, N. Kalra, and N. Khandelwal, "Neural network ensemble based CAD system for focal liver lesions using B- mode ultrasound", *J Digit Imaging*, Vol. 27, No. 4), pp. 520-537, 2014.

[25] J. Virmani, V. Kumar, N. Kalra, and N. Khandelwal, "Prediction of liver cirrhosis based on multiresolution texture descriptors from B- mode ultrasound", *Int J of Convergence Comput*, Vol. 1, No.1, pp. 19-37, 2013.

[26] L. Sandulescu, A. Saftoiu , D. Dumitrescu, and T. Ciurea, "Real-time contrast-enhanced and real-time virtual sonography in the assessment of benign liver lesions", *J Gastrointest Liver Dis*, Vol. 17, No. 4, pp. 475–478, 2008.

[27] M. B. Nielsen, and N. Bang, "Contrast enhanced ultrasound in liver imaging", *Eur J Radiol*, Vol. 51, No. 1, pp. S3–S8, 2004.

[28] F. Minhas, D. Sabih, and M. Hussain, "Automated classification of liver disorders using ultrasound images", *J Med Syst*, Vol. 36, No. 5, pp. 3163–3172, 2011.

[29] C. B. Burckhardt, "Speckle in ultrasound B-mode scans", IEEE Trans. Sonics Ultrason, Vol. SU-25, No. 1, pp. 1- 6, 1978.

[30] R. F. Wagner, S. W. Smith, J. M. Sandrik, and H. Lopez, "Statistics of speckle in ultrasound B-scans", *IEEE Trans. Sonics Ultrason*, Vol. 30 , pp. 156-163, 1983.

[31] C. P. Loizou, C. S. Pattichis, C. I. Christodoulou, R. S. H. Istepanian, M. Pantziaris, and A. Nicolaides, "Comparative evaluation of despeckle filtering in ultrasound imaging of the carotid artery", *IEEE Trans on Ultrasonics*, Vol. 52, No. 10, pp. 1653- 1669, 2005.

[32] D. Sakrison, "On the role of observer and a distortion measure in image transmission", *IEEE Trans Commun*, Vol. 25, No. 1, pp. 1251- 1267, 1997.

[33] W. K. Pratt- *Digital Image Processing*; New York, John Wiley and Sons, 2006.

[34] M. R. Hajiaboli, “An anisotropic fourth-order diffusion filter for image noise removal”, *Int J Comput Vis*, Vol. 92, No. 1, pp. 177- 191, 2011.

[35] Z. Wang, A. Bovik, H. R. Sheikh, and E. P. Semoncelli, “Image quality assessment: From error measurement to structural similarity”, *IEEE Trans. Image Processing*; Vol. 13, No. 4, pp. 600- 612, 2004.

[36] J. S. Lee, “Speckle analysis and smoothing of synthetic aperture radar images”, *Comput. Graph. Image Processing*, Vol. 17, No. 1, pp. 24- 32, 1981.

[37] J. S. Lee, “Digital image enhancement and noise filtering by using local statistics”, *IEEE Trans. Pattern Anal. Machine Intell.*, Vol. PAMI-2, No.2 , pp. 165- 168, 1980.

[38] V. S. Frost, J. A. Stiles, K. S. Shanmuggam, and J. C. Holtzman, “A model for radar images and its application for adaptive digital filtering of multiplicative noise”, *IEEE Trans. Pattern Anal. Machine Intell.*, Vol. 4, No.2 , pp. 157- 165, 1982.

[39] C. Loizou, C. Christodoulou, C. S. Pattichis, R. Istepanian, M. Pantziaris, and A. Nicolaides, ”Speckle reduction in ultrasound images of atherosclerotic carotid plaque”, *IEEE 14th Int. Conf. Digital Signal Processing*, Vol. 2, No. 1, pp. 525-528, 2002.

[40] J. S. Lee, “Refined filtering of image noise using local statistics”, *Comput. Graph. Image Processing*, Vol. 15, No. 1, pp. 380- 389, 1981.

[41] J. S. Lee, “Digital image smoothing and the sigma filter”, *Comput. Graph. Image Processing*, Vol. 24, No. 2, pp. 255-269, 1983.

[42] A. Lopes, TR. Touzi, and E. Nezry, “Adaptive speckle filters and scene heterogeneity”, *IEEE Trans. Geosci. Remote*, Vol. 28, No. 6, pp. 992- 1000, 1990.

[43] D. T. Kuan, A. A. Sawchuk, T. C. Strand, and P. Chavel, “Adaptive restoration of images with speckle”, *IEEE Trans Acoust Speech Signal Processing*, Vol. ASSP-35, pp. 373- 383, 1987.

[44] D. T. Kuan, and A. A. Sawchuk, “Adaptive noise smoothing filter for images with signal dependent noise”, *IEEE Trans Pattern Anal Machine Intell.*, Vol. PAMI-7, No. 2, pp. 165- 177, 1985.

[45] Huang, G. Yang, and G. Tang, “A fast two-dimensional median filtering algorithm”, *IEEE Trans. Acoust. Speech Signal Processing*, Vol. 27, No. 1, pp. 13- 18, 1979.

[46] T. R. Crimmins, “Geometric filter for speckle reduction”, *Applied optics*, Vol. 24, No. 10, pp. 1438- 1443, 1985.

[47] L. Busse, T. R. Crimmins, and J. R. Fienup, ”A model based approach to improve the performance of the geometric filtering speckle reduction algorithm”, *Proc IEEE Ultrason. Symp*, pp. 1353- 1356, 1995.

[48] S. Jin, Y. Wang, and J. Hiller, “An adaptive non-linear diffusion algorithm for filtering medical images”, *IEEE Trans. Inform. Technol. Biomed.*, Vol. 4, No. 4, pp. 298– 305, 2000.

[49] N. Rougon and F. Preteux, “Controlled anisotropic diffusion ”, *SPIE Conf. Nonlinear Image Processing VI, IS&T/SPIE*, San, Vol. 2424, pp. 329– 340, 1995.

[50] M. Black, G. Sapiro, D. Marimont, and D. Heeger, “Robust anisotropic diffusion”, *IEEE Trans. Image Processing*, Vol. 7, No. 3, pp. 421– 432, 1998.

[51] Y. Yongjian, and S. T. Acton, “Speckle reducing anisotropic diffusion”, *IEEE Trans. Image Processing*, Vol. 11, No. 11, pp. 1260– 1270, 2002.

[52] P. Rerona, and J. Malik, “Scale-space and edge detection using anisotropic diffusion”, *IEEE Trans. Pattern Anal. Machine Intell.*, Vol. 12, No. 7, pp. 629– 639, 1990.

[53] D. Gupta, R. S. Anand, and B. Tyagi, “Ripplet domain non-linear filtering for speckle reduction in ultrasound medical images”, *Bio. Signal Processing and Control*, Vol. 10, No. 1, pp. 79- 91, 2014.

[54] S. Sujana, S. Swarnamani, and S. Suresh, “Application of artificial neural networks for the classification of liver lesions by image texture parameters”, *Ultrasound Med Biol*, Vol. 22, No. 9, pp. 1177-1181, 1996.

[55] S. Poonguzhali, Deepalakshmi, and G. Ravindran, “Optimal feature selection and automatic classification of abnormal masses in ultrasound liver images”, *In: Proceedings of IEEE Int Conf on Signal Processing, Communications and Networking, ICSCN’07*, pp. 503-506, 2007.

[56] Y. M. Kadah, A. A. Farag, J. M. Zurada, A. M. Badawi, and A. M. Youssef, “Classification algorithms for quantitative tissue characterization of diffuse liver disease from ultrasound images”, *IEEE Trans Med Imaging*, Vol. 15, No. 4, pp. 466- 478, 1996.

[57] A. M. Badawi, A. S. Derbala, and A. B. M. Youssef, “Fuzzy logic algorithm for quantitative tissue characterization of diffuse liver diseases from ultrasound images”, *Int J Med Inf*, Vol. 55, No. 1, pp. 135- 147, 1999.

[58] K. Fukunaga, “Introduction to Statistical Pattern Recognition”, *Academic, New York*, 1990.

[59] S. H. Kim, J. M. Lee, K. G. Kim, J. H. Kim, J. Y. Lee, J. K. Han, and B. I. Choi, “Computer-aided image analysis of focal hepatic lesions in ultrasonography: preliminary results”, *Abdom Imaging*, Vol. 34, No. 2, pp. 183- 191, 2009.

[60] M. Rachidi, A. Marchadier, C. Gadois, E. Lespessailles, C. Chappard, and C. L. Benhamou, “Laws’ mask descriptors applied to bone texture analysis: an innovative and discrimant tool in osteoporosis”, *Skeletal Radiol*, Vol. 37, No. 1, pp. 541- 548, 2008.

[61] C. J. C. Burges, “A tutorial on support vector machines for pattern recognition”, *Data Min Knowl Disc*, Vol. 2, No. 2, pp. 1- 43, 1998.

[62] I. Guyon, J. Weston, S. Barnhill, and V. Vapnik, “Gene selection for cancer classification using support vector machines”, *J Machine*, Vol. 46, No. 1- 3, pp. 1- 39, 2002.

[63] J. Virmani, V. Kumar, N. Kalra, and N. Khandelwal, “Prediction of cirrhosis from liver ultrasound B-mode images based on Laws’ mask analysis”, *In: Proceedings of the IEEE Int Conf on Image Inf Processing, ICIIP-2011. Himachal Pradesh, India*, pp. 1- 5, 2011.

[64] A. E. Hassanein, and T. H. Kim, “Breast cancer MRI diagnosis approach using support vector machine and pulse coupled neural networks”, *J Applied Logic*, Vol. 10, No. 4, pp. 274-284, 2012.

[65] C. C. Chang, and C. J. Lin, “LIBSVM, a library of support vector machines”, Software available at http://www.csie.ntu.edu.tw/~cjlin/libsvm. Accessed 15 Jan 2015.

[66] S. W. Purnami, A. Embong, J. M. Zain, and S. P. Rahayu SP, “A New Smooth Support Vector Machine and Its Applications in Diabetes Disease Diagnosis”, *J Comput Sci*, Vol. 1, No. 1, pp. 1003-1008, 2009.

[67] Y. J. Lee, and O. L. Mangasarian, “SSVM: A Smooth Support Vector Machine for Classification”, *Computational optimization and Applications*, Vol. 20, No. 1, pp. 5- 22, 2001.

[68] Y. J. Lee, O. L. Mangasarian, “SSVM toolbox”, Software available at http://research.cs.wisc.edu/dmi/svm/ssvm/. 0Accessed 20 Feb 2015.

[69] R. Haralick, K. Shanmugam, and I. Dinstein, “Textural features for image classification”, *IEEE Trans Syst Man Cybern SMC*, Vol. 3, No. 6, pp. 610-121, 1973.

[70] R. M. M. Galloway, “Texture analysis using gray level run lengths”, *Comput Graph Image Process*, Vol. 4, No. 1, pp. 172-179, 1975.

[71] A, Chu, C. M. Sehgal, and J. F. Greenleag, “Use of gray level distribution of run lengths for texture analysis”, *Pattern Recogn Lett*, Vol. 11, No. 1, pp. 415-420, 1990.

[72] B. V. Dasarathy, E. B. Holder, “Image characterizations based on joint gray level-run length distributions”, *Pattern Recogn Lett*, Vol. 12, No. 1, pp. 497-502, 1991.

[73] C. Lee, and S. Chen, “Gabor wavelets and SVM classifier for liver disease classification from CT images”, *In: Proceedings of IEEE Int Conf on Syst, Man and Cybernatics. IEEE, Taipei, Taiwan, San Diego, USA*, pp. 548-552.

[74] K. I. Laws, “Rapid texture identification”, *SPIE Proc Semin Image Process Missile Guid*, Vol. 238, No. 1, pp. 376- 380, 1980.

Appendix-A

Texture Features Used in the Present Work

A.1. Statistical features

A.1.1. First Order Statistics

For the individual pixel values x_i, the computed features are given as:

$$\text{Average Gray Level} = \frac{1}{N}\sum_i x_i$$

$$\text{Standard Deviation} = \frac{1}{\sqrt{N-1}}\left(\sum_i (x_i - \bar{x})^2\right)^{1/2}$$

$$\text{Third Moment} = \frac{1}{N\sigma^3}\sum_i (x_i - \bar{x})^3$$

$$\text{Uniformity} = \sum_i p(i)^2$$

$$\text{Entropy} = -\sum_i p(x_i) log_2 p(x_i)$$

$$\text{Smoothness} = 1 - \frac{1}{1+\sigma^2}$$

A.1.2. GLCM Features

$$\text{Angular Second Moment} = \sum_{i,j} P_{ij}^2$$

$$\text{Contrast} = \sum_{i,j} P_{i,j}(i-j)^2$$

$$\text{Correlation} = \sum_{i,j} P_{i,j}\left[\frac{(i-\mu_i)(j-\mu_j)}{\sigma_i \sigma_j}\right]$$

$$\text{Variance} = \sum_{i,j} P_{i,j}(i-\mu_i)^2$$

$$\text{Inverse Difference moment} = \sum_{i,j} \frac{P_{i,j}}{1+(i-j)^2}$$

$$\text{Sum Average} = f_{12} = \sum_{i=2}^{2N_g} i p_{x+y}(i)$$

$$\text{Sum Entropy} = f_{14} = -\sum_{i=2}^{2N_g} p_{x+y}(i)\log\left(p_{x+y}(i)\right)$$

$$\text{Sum Variance} = f_{13} = \sum_{i=2}^{2N_g} (i - f_{14})^2 p_{x+y}(i)$$

$$\text{Entropy} = -\sum_{i,j} p_{i,j} log(p_{i,j})$$

$$\text{Difference Variance} = -\sum_{i=0}^{N_g-1} (i - f_6)^2\, p_{x-y}(i)$$

$$\text{Difference Entropy} = f_{16} = -\sum_{i=0}^{N_g-1} p_{x-y}(i)\log\left(p_{x-y}(i)\right)$$

$$\text{Information Measure of Correaltion1} = \frac{-\sum_{i,j} p_{i,j}\left(\left(\log(p_{i,j})\right) - \log\left(p_x(i)p_y(i)\right)\right)}{\max\left(HX, HY\right)}$$

$$\text{Information Measure of Correaltion2} = f_{18} = \sqrt{1 - e^{-2(a-b)}}$$

$f_6 = \sum_{i,j} |i - j| p_{ij}$

$a = -\sum_{i,j} p_x(i)p_y(i)\log\left(p_x(i)p_y(i)\right)$

$b = -\sum_{i,j} p_{i,j}\log\left(p_x(i)p_y(i)\right)$

A.1.3. GLRLM Features

$$\text{Short Run Emphasis} = \sum_{i=1}^{G}\sum_{j=1}^{R} \frac{p(i,j|\theta)}{j^2} \Big/ \sum_{i=1}^{G}\sum_{j=1}^{R} p(i,j|\theta)$$

$$\text{Long Run Emphasis} = \sum_{i=1}^{G}\sum_{j=1}^{R} j^2 p(i,j|\theta) \Big/ \sum_{i=1}^{G}\sum_{j=1}^{R} p(i,j|\theta)$$

$$\text{Low Gray level Run Emphasis} = \sum_{i=1}^{G}\sum_{j=1}^{R} \frac{p(i,j|\theta)}{i^2} \Big/ \sum_{i=1}^{G}\sum_{j=1}^{R} p(i,j|\theta)$$

$$\text{High Gray level Run Emphasis} = \sum_{i=1}^{G}\sum_{j=1}^{R} i^2 p(i,j|\theta) \Big/ \sum_{i=1}^{G}\sum_{j=1}^{R} p(i,j|\theta)$$

$$\text{Short Run Low Gray Level Emphasis} = \sum_{i=1}^{G}\sum_{j=1}^{R}\frac{p(i,j|\theta)}{i^2 * j^2} \Big/ \sum_{i=1}^{G}\sum_{j=1}^{R} p(i,j|\theta)$$

$$\text{Short Run High Gray Level Emphasis} = \sum_{i=1}^{G}\sum_{j=1}^{R}\frac{p(i,j|\theta) * i^2}{j^2} \Big/ \sum_{i=1}^{G}\sum_{j=1}^{R} p(i,j|\theta)$$

$$\text{Long Run Low Gray Level Emphasis} = \sum_{i=1}^{G}\sum_{j=1}^{R}\frac{p(i,j|\theta) * j^2}{i^2} \Big/ \sum_{i=1}^{G}\sum_{j=1}^{R} p(i,j|\theta)$$

$$\text{Long Run High Gray Level Emphasis} = \sum_{i=1}^{G}\sum_{j=1}^{R} p(i,j|\theta) * i^2 * j^2 \Big/ \sum_{i=1}^{G}\sum_{j=1}^{R} p(i,j|\theta)$$

$$\text{Gray level Non Uniformity} = \sum_{i=1}^{G}\left(\sum_{j=1}^{R} p(i,j|\theta)\right)^2 \Big/ \sum_{i=1}^{G}\sum_{j=1}^{R} p(i,j|\theta)$$

$$\text{Run Length Non Uniformity} = \sum_{i=1}^{R}\left(\sum_{j=1}^{G} p(i,j|\theta)\right)^2 \Big/ \sum_{i=1}^{G}\sum_{j=1}^{R} p(i,j|\theta)$$

$$\text{Run Percentage} = \frac{1}{n}\sum_{i=1}^{G}\sum_{j=1}^{R} p(i,j|\theta)$$

A.2. Signal Processing Methods based Features

A.2.1. Laws' Texture Features

Laws' masks of lengths 3, 5, 7 and 9 are used to compute different features. As an example Laws' mask of length 3 is used for explanation purposes. The ROIs are convolved with each of the nine 2D Laws' masks.

For example an ROI of size M × N (32 × 32) is convolved with the mask S3S3 to form texture image (TI_{S3S3}).

$$\text{TI}_{\text{S3S3}} = \text{ROI} \otimes \text{S3S3}$$

The mask L5L5 has zero mean and is used to form contrast invariant texture images (TIs).

$$\text{Normalize}(\text{TI}_{\text{mask}}) = \frac{\text{TI}_{\text{mask}}}{\text{TI}_{\text{L3L3}}}$$

The normalized TIs are passed through a 15 × 15 square window to derive 9 texture energy images (TEMs). The TEM filters perform moving average non-linear filtering operation, i.e.

$$TEM_{i,j} = \sum_{u=-7}^{7} \sum_{v=-7}^{7} \left| Normalize(TI_{i+u,j+v}) \right|$$

Out of 9 TEMs 6 rotationally invariant texture energy images (TRs) are obtained by averaging, i.e.

$$TR_{S3L3} = \frac{TEM_{S3L3} + TEM_{L3S3}}{2}$$

Table 1: Description of Laws' masks of different lengths

Length of 1-D filter	1-D filter coefficients	No. of 2D Laws' masks	No. of TR images
3	L3=[1, 2, 1] E3=[-1, 0, 1] S3=[-1, 2, -1]	9	6
5	L5= [1, 4, 6, 4, 1] E5= [-1, -2, 0, 2, 1] S5= [-1, 0, 2, 0, -1] W5= [-1, 2, 0, -2 1] R5= [1, -4, 6, -4, 1]	25	15
7	L7= [1, 6, 15, 20, 15, 6, 1] E7= [-1 -4, -5, 0, 5, 4, 1] S7= [-1, -2, 1, 4, 1, -2, -1]	9	6
9	L9= [1, 8, 28, 56, 70, 56, 28, 8, 1] E9= [1, 4, 4, -4, -10, -4, 4, 4, 1] S9= [1, 0, -4, 0, 6, 0, -4, 0, 1] W9= [1, -4, 4, -4, -10, 4, 4, -4, 1] R9= [1, -8, 28, -56, 70, -56, 28, -8, 1]	25	15

Note: TR: rotation invariant texture images.

From the derived TRs five statistical parameters i.e. mean, standard deviation, skewness, kurtosis and entropy are computed, thus 12 Laws' texture features (6 TRs × 2 statistical parameters) are computed for each ROI. These statistical parameters are defined as:

$$Mean = \frac{\sum_{i=0}^{M} \sum_{j=0}^{N} (TR_{i,j})}{M \times N}$$

$$SD = \sqrt{\frac{\sum_{i=0}^{M} \sum_{j=0}^{N} (TR_{i,j} - Mean)^2}{M \times N}}$$

A.3.2. FPS Features

$$RadialSum = \Phi_{r_1 r_2} = \sum_{r_1^2 \leqslant u^2+v^2 \prec r_2^2} |F(u,v)|^2$$

$$Angular\ Sum = \Phi_{\theta_1,\theta_2} = \sum_{\theta_1 \leqslant \tan^{-1}(v/u) \leqslant \theta_2} |F(u,v)|^2$$

A.3.3. Gabor Filter based Features

$$Mean = \frac{1}{m}\sum_{i} iP_{ij}$$

$$\text{Variance} = \sum_{i,j} P_{i,j}(i-\mu_i)^2$$

Appendix-B

Plagiarism Report of the Present Work

ORIGINALITY REPORT

10 %	2 %	10 %	0 %
SIMILARITY INDEX	INTERNET SOURCES	PUBLICATIONS	STUDENT PAPERS

S. No.	Title (Source)	Plagiarism
1	Edwards, K.. "An evaluation of bifocal lens performance and the design of a new fitting protocol", Journal of the British Contact Lens Association, 1987. (Publication)	2 %
2	Virmani, Jitendra, Vinod Kumar, Naveen Kalra, and Niranjan Khandelwal. "SVM-based characterisation of liver cirrhosis by singular value decomposition of GLCM matrix", International Journal of Artificial Intelligence and Soft Computing, 2013. (Publication)	2 %
3	Virmani, Jitendra, Vinod Kumar, Naveen Kalra, and Niranjan Khandelwal. "Prediction of liver cirrhosis based on multiresolution texture descriptors from B-mode ultrasound", International Journal of Convergence Computing, 2013. (Publication)	1 %
4	Mittal, D. "Neural network based focal liver lesion diagnosis using ultrasound images",Computerized Medical Imaging and Graphics,201106. (Publication)	1 %
5	momed.king.ac.uk (Internet Source)	1 %
6	Jitendra Virmani. "Prediction of cirrhosis from liver ultrasound B-mode images based on Laws' masks analysis", 2011 International Conference on Image Information Processing, 11/201. (Publication)	1 %
7	C.P. Loizou. "Comparative evaluation of despeckle filtering in ultrasound imaging of the carotid artery", IEEE Transactions on Ultrasonics Ferroelectrics and Frequency Control, 10/2005. (Publication)	< 1 %
8	Yeh, W.C.. "Liver fibrosis grade classification with B-mode ultrasound", Ultrasound in Medicine & Biology, 200309. (Publication)	< 1 %
9	www.ito.umnw.ethz.ch (Internet Source)	< 1 %
10	Hiroyuki Yoshida. "Wavelet-packet-based texture analysis for differentiation between benign and malignant liver tumours in ultrasound images", Physics in Medicine and Biology, 11/21/2003. (Publication)	< 1 %
11	Suzuki, K.. "Dependence of ultrasonic attenuation of liver on pathologic fat and fibrosis: Examination with experimental fatty liver and liver fibrosis models", Ultrasound in Medicine & Biology, 1992. (Publication)	< 1 %
12	g.lemaitre58.free.fr (Internet Source)	< 1 %
13	www.apforum.org (Internet Source)	< 1 %

14	Chu, Yong, Lihua Li, Dmitry B. Goldgof, Yan Qui, Robert A. Clark, and J. Michael Fitzpatrick.", Medical Imaging 2003 Image Processing, 2003. (Publication)	< 1 %
15	Aylward, Stephen, Lubomir M. Hadjiiski, Simranjit Kaur, Vipul Sharma, Sukhwinder Singh, and Savita Gupta. "A content based framework for mass retrieval in mammograms", Medical Imaging 2014 Computer-Aided Diagnosis, 2014. (Publication)	< 1 %
16	Christos P. Loizou. "Despeckle Filtering of Ultrasound Images", Atherosclerosis Disease <1% Management, 2011. (Publication)	< 1 %
17	Jitendra Virmani. "Prediction of Cirrhosis Based on Singular Value Decomposition of Gray Level Co-occurence Marix and Neural Network Classifier", 2011 Developments in E-systems Engineering, 12/2011, (Publication)	< 1 %
18	A.K. Chong. "Computer Assisted Surgical Planner for Craniofacial Reconstruction -Imaging Techniques", Geometric Modeling and Imaging--New Trends (GMAI 06), 2006, (Publication)	< 1 %
19	kaskusjualbeli.net (Internet Source)	< 1 %
20	biosim.ece.ntua.gr (Internet Source)	< 1 %
21	Wu, C.H.. "Segmentation of kidney from ultrasound B-mode images with texture-based classification", Computer Methods and Programs in Biomedicine, 200612. (Publication)	< 1 %
22	Hamid R. Tizhoosh. "Increasing segmentation accuracy in ultrasound imaging using filtering and snakes", 2008 Canadian Conference on Electrical and Computer Engineering, 05/2008. (Publication)	< 1 %
23	Thomas C. Gerber. "Differentiation of Intracardiac Tumors and Thrombi by Echocardiography Tissue Characterization: Comparison of an Artificial Neural Network and Human Observers", Echocardiography, 2/2000. (Publication)	
24	Joongkyu Choi. "A stochastic multi-item inventory model with unequal replenishment intervals and limited warehouse capacity", IIE Transactions, 12/1/2005. (Publication)	< 1 %
25	Al-Osta, Husam E. I.(Ipson, Stanley S. and Qahwaji, Rami S. R.). "Detection of breast cancer microcalcifications in digitized mammograms. Developing segmentation and classification techniques for the processing of MIAS database mammograms based on the Wavelet Decomposition Transform and Support Vector Machines.", University of Bradford, 2010. (Publication)	< 1 %
26	Pakkurthi Srinivasu. "A Modified Kolmogorov Smirnov Correlation Based Filter Algorithm for Feature Selection", Advances in Intelligent and Soft Computing, 2012. (Publication)	< 1 %
27	Miha Smolnikar. "Propagation Impairment Countermeasures in Mobile Stratospheric Operating Environment", VTC Spring 2009 - IEEE 69th	< 1 %

	Vehicular Technology Conference, 04/2009. (Publication)	
28	Jianmin Dong. "A novel smooth Support Vector Machines for classification and regression", 2009 4th International Conference on Computer Science & Education, 07/2009. (Publication)	< 1 %
29	www.global-help.org (Internet Source)	< 1 %
30	G.A. Tsihrintzis. "A Middleware System for Web-Based Digital Music Libraries", The 2005 IEEE/WIC/ACM International Conference on Web Intelligence (WI 05), 2005. (Publication)	< 1 %
31	Tolba, A. S., H. A. Khan, A. M. Mutawa, and S. M. Alsaleem. "Decision Fusion for Visual Inspection of Textiles", Textile Research Journal, 2010. (Publication)	< 1 %